

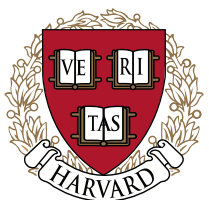
Master's Thesis

# Dynamic Holography and Beamshaping using Digital Micromirror Devices



**Philip P. J. Zupancic**  
Ludwig-Maximilians-Universität München  
2013

**Prof. Dr. Markus Greiner**  
Harvard-MIT Center for Ultracold Atoms  
Harvard University  
**Primary Advisor**



**Prof. Dr. Immanuel F. Bloch**  
Max-Planck-Institute for Quantum Optics /  
Ludwig-Maximilians-Universität München  
**Secondary Advisor**





German title:

## **Dynamische Holographie und Strahlformung mittels digitaler Mikrospiegelaktoren**

### **Abstract**

I present a robust scheme to measure and compensate phase front distortions of laser systems in-situ using a digital micromirror device as a holographic spatial light modulator. The detectors for the measurements can be ultracold atoms in optical lattices, trapped ions, NV centers or other small, localized and fluorescent objects. With this, aberrations of several  $\lambda$  can be reduced to  $\lambda/50$ . This gives rise to diffraction-limited spot sizes, e.g. to address single atoms in a periodic potential. Furthermore, arbitrary potential landscapes can be created and steered dynamically with high precision.



*Dedicated to  
my parents  
for their love and support  
over the years*



# Contents

<b>Introduction</b>	<b>2</b>
<b>1 Let there be light</b>	<b>5</b>
<b>2 Spatial Light Modulation</b>	<b>15</b>
2.1 Tools . . . . .	15
2.2 Amplitude Holograms . . . . .	19
2.3 Beamshaping . . . . .	22
<b>3 Holographic Beamshaping</b>	<b>24</b>
3.1 Analytical Beam Optimization . . . . .	24
3.2 First Experimental Results . . . . .	33
3.3 Advanced Beamshaping . . . . .	39
<b>4 High-NA Applications</b>	<b>45</b>
4.1 Preliminary Considerations . . . . .	45
4.2 Fluorescent Microspheres . . . . .	47
4.3 Quantum Gas Microscope . . . . .	49
<b>Conclusion</b>	<b>55</b>
<b>Appendices</b>	<b>57</b>
<b>A Dressed State Picture</b>	<b>58</b>
<b>B The 30-minute Guide to Fourier Optics</b>	<b>62</b>
<b>Bibliography</b>	<b>73</b>
<b>Acknowledgement</b>	<b>75</b>

# Introduction

Today's high-performance computers can run real-time simulations of entire organisms on a molecular level[1], reconstruct the evolution of structure in the universe from the Big Bang to now[2] or simulate the changing climate on planet Earth.[3] Even our cell phones are a million times more powerful than the computer that brought the Apollo 11 crew to the moon and back. But we can not calculate the dynamics of a strongly correlated quantum system with more than a few particles, because the computational resources required for quantum problems scale exponentially with the number of parts involved. It has been more than thirty years since Richard Feynman presented his idea of a quantum simulator to work around the intrinsic limitations of classical computers in solving these problems.[4] But why is that interesting?

The basic method of science is to predict the outcome of an experiment based on a hypothesis, and evaluate the hypothesis according to its deviation from reality. Unfortunately, we cannot predict the outcome of an experiment if we do not have the processing power to calculate the evolution of the system in question. Quantum field theories are among the most fundamental theories physicists are working on, but we have a hard time solving their equations for many-body systems, so that it is difficult to test models, e.g. for high-T<sub>C</sub> superconductors or the evolution of the early universe. Quantum simulation offers a way out of this dilemma, since questions about an unfamiliar quantum system A can be answered by making a well-understood quantum system B look just like it.

But quantum simulation is also closely related to quantum computation. Here, Hamiltonians are engineered to implement a quantum-mechanical “flowchart”, i.e. a network of quantum gates that are similar to classical gates but preserve properties like entanglement. This way, an input quantum state can be processed coherently into an output state. We are still lacking mathematical proofs, but there appears to be a class of problems, called *NP problems*, that cannot be solved efficiently on classical computers, like integer factorization or the traveling salesman problem. However, the complexity class of quantum computers is at least a subset of this class, so that some, if not all, of these NP problems can indeed be solved on such devices.[5] A universal quantum computer would be a giant leap in our computational abilities, and would have a major impact on science and society.

The word of quantum simulation and computation has been around since 1981. So where are we with that? Current candidates for quantum simulators include cold atoms and molecules[6], trapped ions[7], nitrogen-vacancy centers in diamonds[8] or photonic systems[9], i.e. all few-particle or many-particle quantum systems that we have a good degree of control over. The key to all of

those systems is the interaction of light with matter, so that a complete toolbox of well-established high-precision techniques can be borrowed from the field of experimental quantum optics in order to achieve the desired system qualities.

A demonstration of quantum simulation from our lab in the field of ultracold atoms is the implementation of an antiferromagnetic chain of spin-1/2 particles in a system of spinless bosons. For this, a two-dimensional gas of Rubidium atoms in an optical lattice is separated into one-dimensional tubes by modifying the lattice shape. The fermionic spin dynamics are then emulated by the generation of an external field, which tilts the potential landscape. Since multiple occupation of one lattice site costs energy in the presence of interactions and tunneling has to preserve energy, tunneling along the potential gradient is allowed or prohibited based on the occupation of the target lattice site, and can thus favor or avoid double occupation depending on the energy gradient. The resulting atom number distribution can be mapped onto spin  $\pm 1/2$  in perfect agreement with calculations on the Ising model.[10]

This and other examples are great demonstrations of engineering Hamiltonians. The pursuit of a *universal* quantum simulator, however, is still far from satisfied. The challenge is to prepare many-body-systems in any desired state and engineer an arbitrary Hamiltonian to govern their dynamics, let the system evolve and measure the result. Light plays a paramount role in cold atom physics and related subjects, since light fields can change internal states by inducing transitions and act as potentials via the AC-Stark shift. Thus, both afore-mentioned challenges can be faced with appropriate control over laser parameters. Unfortunately, this is really hard.

What makes it so difficult is the demand on precision. Typical spacings in optical lattice experiments are on the order of half the diffraction-limited spot size of a laser beam. For the preparation of an internal state it is necessary to address single atoms without affecting its neighbors. To achieve this, no aberrations can be in the imaging system and the addressing beam must be precisely aligned and steerable with the lattice.[11]

The next challenge is to bring a laser beam into a shape accurately resembling the potential of the Hamiltonian that is to be engineered. The idea behind dynamical beamshaping is to use an electronically controlled device of hundreds of thousands of elements on a two-dimensional grid whose transmittance or reflectivity can be set individually, such as liquid-crystal displays or digital micromirror devices.

In this work I will present my research on the holographic employment of such devices to cancel aberrations and create high-precision beam profiles. The solution is highly flexible and allows the creation of arbitrary beam shapes. In certain domains, the achieved accuracy is considerably higher than any techniques presented and used so far.

Adaptive optics is not exactly a new field - first proposed in the 1950s and becoming reality thirty years later, deformable mirrors have been around for two decades. With the advancements of liquid-crystal technology and microelectromechanical devices, holographic phase correction and measurement was researched in the last few years. Most detection schemes are based on laser speckle correlations on CCD cameras[12, 13, 14, 15], and are not ideally suited for cold atom experiments. Digital micromirror devices have also been used for beamshaping, both in direct imaging[16] and holographically[17].

The novelty in our approach is to combine adaptive optics with beamshaping,

and to measure phase and amplitude profiles of our beam *in-situ* and *exactly*, similar to a technique by the Dholakia group[18]. This means, that any wave-front distortions are measured in the precise location of the experiment using fluorescence from the atoms in the optical lattice to directly measure local phases instead of using iterative corrections. Based on the measured profile, patterns can be created to cancel aberrations up to an rms phase error of  $\lambda/50$ . Beam profiles can be generated with signal-to-noise ratios of up to  $10^4$ . The technique is ideally suited for small, precise features that require a high degree of control over beam direction and shape in experiments on ultracold atoms and related fields.

In the first chapter, I recap some fundamental results from atomic physics and optics that are important for this thesis. I briefly cover light-atom interactions with the application for quantum gas microscopes and give an introduction to Fourier optics, with more detailed derivations in the two appendices. The second chapter is about general aspects of beam shaping and discusses two classes of devices that can be used in its realization.

The subsequent chapter is the centerpiece of the thesis and is dedicated to the phase and amplitude mapping sequence that gives rise to the high quality shapes that were mentioned before. It also contains the most important results in terms of beamshaping capabilities and several examples from a test setup.

The final chapter discusses the transition to real-life applications at high numerical apertures and shows results from our quantum gas microscope.

# Chapter 1

## Let there be light

### Lasers in Atomic Physics

Light has always been the scientists' best friend - it allows us to observe the natural world around us. We explored *optics* to understand propagation phenomena so that we could build microscopes and telescopes and expand our reach to ever smaller or more distant objects. Collecting and processing emitted or scattered light from the studied objects is still an important part of most natural sciences. But since the advent of lasers in the 1950s, the *active* use of light has opened many more doors. Light interacts with matter in a complex way that gives rise to manifold applications, especially when good control over frequency, phase and intensity is available. In this section I will briefly review some basics of atom-light interaction and explain some of its applications in the experimental setup of a quantum gas microscope.

The most important light-atom-interaction is the *dipole* interaction. An atom in the ground state has no electric dipole moment on average. If you place this atom in a light field with frequency  $\omega$ , the electric field  $E$  will induce an electric dipole moment  $p$ , oscillating with the same frequency  $\omega$ . If  $\omega$  is close to an electronic transition in the atom at  $\omega_0$ , the atom can absorb a photon from the light field and be excited to a higher energy level. This process can also be inverted: in a near-resonant, coherent light-field, an atom in an excited state can be stimulated to emit a photon back into the light field. Actually, the atom will change coherently from the groundstate through superposition states into the excited state and back. This behaviour is called *Rabi oscillation*.[19]

The induced dipole moment will be proportional to the driving field,

$$p = \alpha \cdot E, \quad (1.1)$$

where  $\alpha = \alpha(\omega)$  is the polarizability of the atom at frequency  $\omega$ . If the driving frequency  $\omega$  and the atomic transition frequency  $\omega_0$  are detuned, the dipole interaction will mostly be dispersive, which means that there is only a small chance of an absorption event. Instead, the electric field will interact with the induced dipole moment and shift the level of the atom by the dipole potential

$$U_{\text{dip}} = -\frac{1}{2} \langle pE \rangle \propto \Re(\alpha)E^2. [20] \quad (1.2)$$

A gradient in the dipole potential will lead to a conservative force acting on the atoms. The polarizability  $\alpha$  will be either positive or negative, depending

on the sign of the detuning  $\delta = \omega - \omega_0$ , so that the force

$$F_{\text{dip}} = -\nabla U_{\text{dip}} \quad (1.3)$$

will act towards regions of high intensity for red-detuned light fields ( $\omega < \omega_0$ ) or away from them for blue-detuned light ( $\omega > \omega_0$ ). Both Rabi oscillations and the dipole potential are derived more rigorously in Appendix A in the framework of “dressed” two-level-systems.

The dipole potential is proportional to  $E^2$ . And, most conveniently, so is the light intensity  $I$ . This means that the intensity distribution of the light field, i.e. the profile of the applied laser beam, will directly correspond to the potential seen by the atoms. This can be used to trap neutral atoms in vacuum, either by keeping them in the focus of a red-detuned laser beam, where the intensity is highest (*dipole trap*), or by confining them in a minimum of a blue-detuned light field.

## Quantum Gas Microscope

The main apparatus that is run in our group is a quantum gas microscope. In this setup several stages of laser cooling, optical pumping and evaporative cooling are applied to produce a degenerate quantum gas (*Bose-Einstein-Condensate* or BEC) of  $5 \cdot 10^4$  ultracold Rubidium-87 atoms in the  $F = 1$ ,  $m_F = -1$  state at a few nK.[21, 22]

It would be inappropriate to cover the full cooling procedure in much detail here. But I would like to illustrate some basics for readers unfamiliar with the concept. The first and the last step of the sequence should convey the general idea.

The first step is a *magneto-optical trap* (MOT), that loads a vapor gas at ambient temperature into a trap and cools it down to  $100 \mu\text{K}$ . The MOT consists of six laser beams of the same frequency, that are red-detuned with respect to a hyperfine transition and a pair of coils in an anti-Helmholtz configuration (parallel coils that are one radius apart, with currents running in opposite directions). The coils produce a magnetic field that is zero in the center and rises linearly going away from it.

The energy levels of the atoms are subject to the Zeeman-shift in presence of magnetic fields[23]. This shift brings the red-detuned laser light close to resonance when an atom is moving out of the central region, so that the escaping atom can be excited. Since photons carry a momentum  $\hbar k$ , the atom will get a momentum kick back towards the center from the absorption event. Later it will decay spontaneously with another momentum transfer, but in a random direction. If many absorption-spontaneous-emission cycles happen, the atom experiences a considerable net force towards the center of the trap. The polarization of the laser beams is chosen so that atoms can only absorb photons that are moving in opposite directions (fig. 1.1). This kind of trap can cool atoms down to a temperature on the order of the *recoil energy*, that is the energy associated with the momentum exchange of single photons.[19] There is a wide variety of techniques using directed momentum transfer from photons to atoms, which can be found in the standard textbooks.

The other technique that I want to mention is called *evaporative cooling* and is necessary to bring the temperature way below the recoil limit and into a regime of degeneracy. There is a thermal distribution of kinetic energies in the

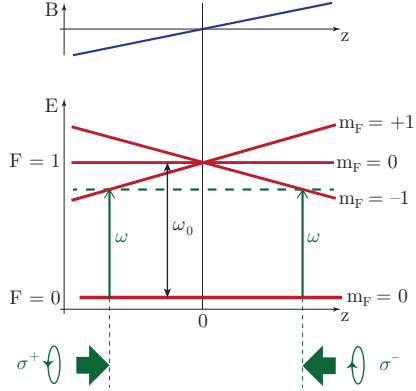


Figure 1.1: Energy levels in a MOT. The lasers are set up to be in resonance with  $|m_F| = 1$  states away from the center, so that escaping atoms get a momentum kick from the absorption, forcing them back to the center and cooling them down.

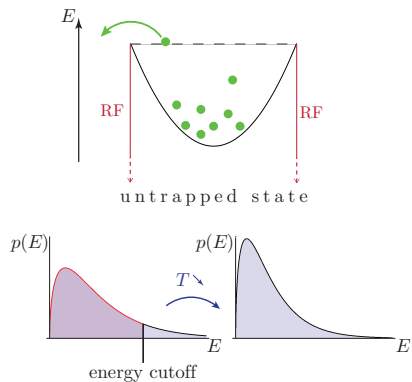


Figure 1.2: The idea of evaporative cooling is to eject atoms with above-average energy, so that the system rethermalizes at lower temperatures with each ejection event. This is done by inducing an RF transition at a high threshold energy.

atomic cloud. The idea is to expel atoms with kinetic energy above average, so that the gas rethermalizes at a lower energy after each ejection event. This can be realized by a trap potential with e.g. a quadratic shape, and with a “hole” at a certain energy level. This can be done by applying a strong RF signal tuned to a frequency, so that atoms far from the center of the trap will get in resonance with this frequency. They get excited into an untrapped state and are lost from the trap. Performed correctly, this technique can bring the gas to temperatures of few nanokelvin (fig. 1.2).[21]

After cooling down to the point where a BEC is created, the atoms are loaded into an *optical lattice*. An optical lattice is a periodic potential (fig. 1.3) created by a spatially oscillating light field that is blue-detuned with respect to an electronic transition. This potential localizes the atoms, and can trap them at a sufficient depth, too. It can be generated in two ways: either by counter-propagating laser beams of the same frequency, polarization and intensity (e.g. a retro-reflected beam) that form a standing wave, or by holographically projecting the desired profile onto the atoms, as it is done in our experiment.

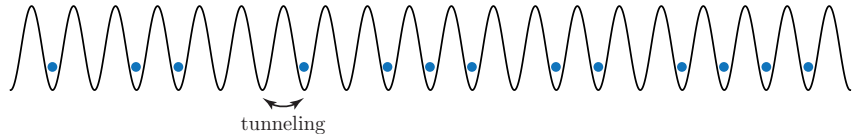


Figure 1.3: One-dimensional optical lattice.

The dynamics of the trapped atomic cloud strongly depend on the depth of the lattice-potential and thus on the laser intensity. In a deep potential, atoms are well localized (so-called *Mott insulator*), while a shallow lattice allows

tunneling between neighboring lattice sites (*superfluid*).[24] At the same time, interactions between atoms can be tuned magnetically via *Feshbach Resonances* over several orders of magnitude.[25, ch. 5]

The special aspect of a quantum gas microscope is an objective with an imaging performance high enough to resolve single lattice sites. This way, not only collective properties of the gas, but also individual atom positions and properties such as spin can be measured.[26] At the same time the imaging system allows to focus a laser to a spot size comparable to the lattice spacing, so that individual atoms can be addressed, e.g. to flip their spins.[11]. Single-site detection and addressing make the quantum gas microscope a promising candidate for universal *quantum simulators* and *quantum computers*.[6]

Calculations for quantum many-body systems are computationally very hard, because the dimensionality of the phase space and thus the amount of required memory and processing power scales exponentially with the number of particles, compared to the linear scaling in a classical system. Richard Feynman suggested in 1982 that people should use quantum systems to solve quantum problems in order to circumvent the limitations of classical computers.[4] The idea is to have a quantum many-body system, in which

- an arbitrary initial state can be prepared,
- a Hamiltonian for single particles and their interactions can be engineered
- quantum coherence is preserved over sufficient time scales, and
- the resulting dynamical properties can be measured time- and space-resolved with high fidelity. (DiVincenzo criteria[27])

This system can then be utilized to simulate the behavior of another quantum system, that can be completely different in nature and that can possibly neither be observed nor calculated. The idea, in a nutshell, is to make a well understood and well controlled quantum system A look and behave like a system B that we cannot control and do not understand, and hopefully learn something about B by studying the dynamics of A.[28].

A quantum computer is a somewhat similar device. It uses the exponentially growing phase space of a quantum system to solve problems of a high complexity class like NP (the computation time for the solution to a problem of this class scales non-polynomial with the number of parameters).[29] Typical examples for this class of problems are integer factorization or graph coloring, in which the vertices of a graph need to be colored such that no two adjacent vertices share the same color. Just as a quantum simulator, a quantum computer needs the ability to tune interactions and Hamiltonians. In analogy to classical computers, where bits are processed in gates, the Hamiltonians engineered in quantum computers shall implement gates that coherently act on quantum bits, or *qubits*. Since these qubits can be in any superposition of 0 and 1 and can be entangled with each other, a quantum computer might be able to process any number of input states simultaneously. For example, there exist quantum algorithms for integer factorization and database searches, that scale polynomially in contrast to their classical counterparts.[29] The former one has been successfully implemented on a 5-qubit-system a decade ago.[5]

An optical lattice experiment is particularly well-suited for simulations of condensed matter systems that share the periodic structure. Optical lattices

can be created with different structures[30, 16, 31], and the atoms inherit the corresponding band structure. Another application are so-called *lattice gauge fields*. These are discretized model systems for high-energy quantum field theories like potentially QED (quantum electrodynamics) or QCD (quantum chromodynamics), that can be studied in a quantum simulator.[32]

The hope of many cold atom physicists is that an optical lattice experiment can be used as a *universal* quantum simulation at some point. I have listed some requirements before. This thesis is mostly about achieving the first two aspects, preparation of an initial state and engineering of Hamiltonians. I have pointed out that light can change the internal state of an atom or that it can act as a potential, depending on the frequency. So the question that I will try to answer in this work is: how do you perform high-precision modulations on laser beam profiles to create arbitrary potential landscapes or prepare states?

## Optical challenges

Unfortunately, the performance of all optical systems is limited for both technical and fundamental reasons. Let us start with the latter.

Comparing a Fourier transform

$$\mathfrak{F}\{g(x, y)\}(f_X, f_Y) = \int_{\mathbb{R}^2} g(x, y) \exp(-i2\pi(f_X x + f_Y y)) dx dy \quad (1.4)$$

with the propagation of a plane wave

$$p(x, y) = a \exp(i(k_X x + k_Y y)), \quad (1.5)$$

one could say that the function  $g(x, y)$  is decomposed into a spectrum of (physical) plane waves. *Fourier Optics* is concerned with this plane wave spectrum, and many results concerning diffraction and optical performance can be derived from its propagation.[19]

Starting with some light field distribution in the object plane of an optical system, the Fourier components of this light field propagate as plane waves in different directions. If the object is in the focal plane of a collimation lens, this lens translates different angles into different positions within the collimated beam. Thus, the profile of the collimated beam corresponds to the Fourier transform of the light field in the object plane, up to phase curvature. The phase curvature disappears in the second focal plane, which got the name *Fourier plane* for this reason.

Fourier components correspond to angles, which are translated into positions. But the extent of the optical system is limited by the aperture. Thus, only frequencies below a certain threshold can propagate through the imaging system. This threshold is given by the largest angle  $\theta_m$  that can be collected by the entrance pupil, or the *numerical aperture* (NA) of the system, defined as

$$NA = n \sin(\theta_m) \quad (1.6)$$

where  $n$  is the index of refraction. This frequency cutoff defines the performance of the imaging.

The propagation of light is governed by the Helmholtz equation

$$\nabla^2 U(\vec{r}) + k^2 U(\vec{r}) = 0. \quad (1.7)$$

Since this differential equation is linear, an imaging setup can be treated as a linear system, so that the image of an object can be calculated as the sum of the images of all point sources on the object. The response of the system to a point source is called *point-spread function* (PSF). A perfect imaging system collects all light from an object up to the threshold angle given by the NA, passes it through a number of lenses and turns the light into spherical waves converging on the image plane. In this case, the PSF will be the Fourier transform (or the far-field diffraction pattern) of the aperture, and the imaging system is called *diffraction-limited*. This means it is limited *only* by aberrations, and not by imperfections of optics or other faults. Appendix B contains a more detailed derivation of the angular spectrum approach in Fourier optics and the aforementioned results.

The condition for ideal performance, as defined previously, is a perfectly spherical outgoing wave. Deviation from the spherical phase profile leads to a decreased imaging performance, i.e. a larger spreading in the impulse response. Though this can be proven rigorously[33, ch. 6.4], a simple argument should suffice for our purposes: If the phase profile is spherical, then all parts of the beam interfere constructively at one point in the image plane, giving rise to a well defined maximum. In the case of phase distortions the interference is less than 100% constructive or even destructive, reducing the central intensity. But since the intensity is a measure of energy and thus conserved, the remaining power has to be redistributed, which leads to a blurring in the PSF. These distortions are called *aberrations*.

Since the laser light used in experiments in atomic physics is monochromatic, so-called *chromatic* aberrations that stem from the wavelength-dependent refractive index will not be considered here. Rather important are aberrations that are due to errors made in the paraxial approximation that is used in the derivation of geometrical optics,

$$\sin \phi = \phi - \frac{\phi^3}{3!} + \frac{\phi^5}{5!} + \mathcal{O}(\phi^7) \approx \phi \quad (1.8)$$

where  $\phi$  is the angle between a beam and the optical axis. Most results from geometrical optics like the lens equation are only valid to this approximation.

We will mostly be interested in corrections up to third order in  $\phi$ . These aberrations are called *Seidel* aberrations:

- *Astigmatism.* This is an anisotropic effect that gives rays in two perpendicular planes different foci. This aberration can be significant when cylindrical lenses are used (i.e. lenses that focus light only along one axis).
- *Coma.* Comatic aberrations describe a variation in magnification over the entrance pupil, so that it affects off-axis points on the object. It leads to a comet-like tail.
- *Spherical aberrations.* In contrast to 1<sup>st</sup> order geometrical optics, spherical surfaces do not create a perfect spherical phase profile. The result is, that rays parallel to the optical axis at different radii will have different focal planes.
- *Field curvature* and *Distortion*. These do not effect the shape of the impulse response in the image plane, but rather change the geometry of

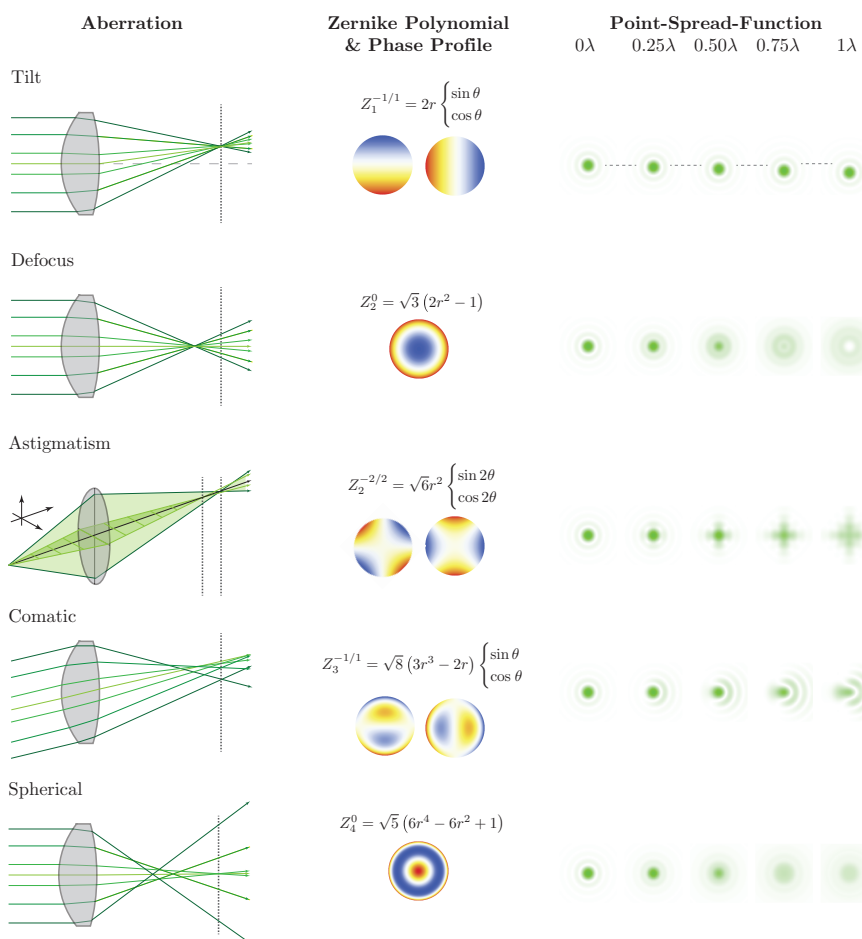


Figure 1.4: Low-order aberrations and their effects on wave fronts and the PSF for different peak-to-peak strengths from 0 to 1 wavelength of distortion.

the image plane. They are relevant only for widely extended images with respect to the focal length, so that they will play no role in the application for optical lattice experiments.

A more obvious kind of aberration is defocus. Defocus means that wave fronts are converging properly, but not to a point in the desired plane. As explained before, a converging spherical wave is the result of a spherical phase profile behind the last lens. In the case of defocus, there is a profile like that, but with an incorrect parameter. According to eq. B.25, the phase error is

$$\Delta\phi(x, y) = \phi(x, y, 0) - \phi'(x, y) = \frac{k}{2} \left( \frac{1}{f^2} - \frac{1}{f'^2} \right) (x^2 + y^2) \quad (1.9)$$

where  $f$  is the design focal length and  $f'$  the actual one. Thus, in good approximation defocus leads to a quadratic phase factor.

The concept of defocus can be extended to a displacement in the transverse direction. Since the direction of propagation is defined by the normal vector to the phase front, tilting the phase front will change the location of the focal point. A tilt corresponds to a linear slope. It is not considered a real aberration, since it does not bend the wave fronts.

All these imaging errors are illustrated in fig. 1.4 with their effect on the phase profile and the point-spread-function.

A mathematically convenient way to describe aberrations are Zernike polynomials. They form a complete, orthogonal set of functions on the unit circle and each of the (lower order) polynomials corresponds to one particular kind of aberrations. They are defined as

$$Z_n^{\pm m}(r, \phi) = R_n^m(r) \begin{cases} \cos(m\phi) & \text{for even } m \\ \sin(m\phi) & \text{for odd } m \end{cases} \quad (1.10)$$

and

$$R_n^m(r) = \sum_{k=0}^{(n-m)/2} \frac{(-1)^k (n-k)!}{k! ((n+m)/2 - k)! ((n-m)/2 - k)!} r^{n-2k} \quad (1.11)$$

To visualize the effect of aberrations on the phase front, the relevant Zernike polynomials are printed and plotted with the aberrations in fig. 1.4. (In order to be orthonormal, Zernike polynomials do not represent the actual phase error - instead, the projection of the wave front onto a Zernike polynomial is proportional to the aberration described by it. E.g., a spherical aberration is a pure  $r^4$ .)

One of the main goals of this project is to cancel third order aberrations and defocus in order to get diffraction-limited performance in applications that require high imaging resolutions, such as single-site addressing in optical lattices. The process of measuring phase distortions and compensating for them will be discussed in the next chapters.

Tilt will be particularly important for the dynamical beamshaping that is utilized later on. Third order aberrations are inherent to the optical components and will be constant over time, so that their undesirable effects can be canceled. Tilt on the other hand can be considered a tool, since it can be a helpful degree of freedom. Beams can be steered to address different positions in the image

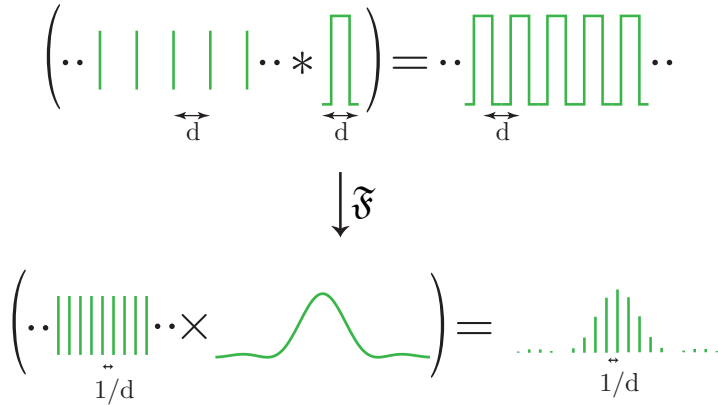


Figure 1.5: Mathematically, a grating is the convolution of a Dirac comb and a single slit. This figure illustrates this relation in the space domain and the Fourier domain.

plane by changing the tilt, such as different lattice sites in the quantum gas microscope.

In summary, all imperfections in an optical system introduce a corresponding phase distortion to the wave fronts emerging from it, which can be described by a polynomial. This has an important implication to the overall phase profile: Since polynomials are smooth, the phase profile can be expected to be smooth, too. This will be a critical condition when it comes to the measurement of aberrations.

## Diffraktion

Diffraktion will be particularly important in this thesis. Firstly, because it defines the shape of the point-spread function from the usually circular aperture, and secondly, because diffraction gratings play a major role in our beamshaping scheme. The diffraction pattern of the first one is readily found to be[33, ch. 2]

$$I(\theta) = I_0 \left( \frac{2J_1(ka \sin \theta)}{ka \sin \theta} \right)^2 \quad (1.12)$$

where  $J_1(x)$  is the Bessel function of first kind of order one,  $a$  is the radius of the aperture and  $\theta$  is the propagation angle. This pattern is called Airy disk.

A (one-dimensional) diffraction grating is a periodic structure of alternating transparent and opaque slits. Mathematically it can be described as the convolution of a single slit with a comb of  $\delta$ -distributions, centrally putting the slits onto the comb (fig. 1.5)[34]. In terms of frequency space and angular spectrum ( $f_X = \alpha/\lambda$  where  $\alpha$  is a direction cosine) these functions translate to

$$\mathfrak{F} \left\{ \text{rect} \left( \frac{x}{a} \right) \right\} = \frac{1}{a} \text{sinc}(af_X) = \frac{1}{a} \text{sinc} \left( a \frac{\alpha}{\lambda} \right) \quad (1.13)$$

with

$$\text{rect}(x) = \begin{cases} 1 & \text{if } x < \frac{1}{2} \\ 0 & \text{else} \end{cases} \quad (1.14)$$

and

$$\begin{aligned}
 \mathfrak{F} \left\{ \sum_{n=-\infty}^{\infty} \delta(x - nd) \right\} &= \frac{1}{d} \sum_{m=-\infty}^{\infty} \delta \left( f_X - \frac{m}{d} \right) \\
 &= \frac{1}{d} \sum_{m=-\infty}^{\infty} \delta \left( \frac{1}{\lambda} \left( \alpha - \frac{m\lambda}{d} \right) \right) \\
 &= \frac{\lambda}{d} \sum_{m=-\infty}^{\infty} \delta \left( \alpha - \frac{m\lambda}{d} \right), \tag{1.15}
 \end{aligned}$$

so that the angular spectrum of a grating is a comb with reciprocal spacing  $\lambda/d$  and an envelope given by the single-slit diffraction pattern (fig. 1.5).  $\alpha$  is the direction cosine of the angle  $\theta'$  between the plane wave normal and the grating surface,  $\alpha = \cos \theta'$ , so that the angle relative to the grating normal is  $\theta = \pi/2 - \theta'$  and we have  $\alpha = \sin \theta$ . Inserting this into eq. 1.15 yields the *grating equation*

$$d \sin \theta_m = m\lambda \tag{1.16}$$

that gives us the angles of local maxima in the angular spectrum and thus in the far-field diffraction pattern. The number  $m$  is called the *diffraction order*. For the more general case of illumination at an angle  $\theta_i$ , eq. 2.3 becomes

$$d(\sin \theta_i + \sin \theta_m) = m\lambda. \tag{1.17}$$

(Our result is not physical since the diffraction orders are still described by a Dirac comb. This stems from our neglecting of the finite extent of the illuminating beam. In a realistic situation, only  $N$  grating slits will contribute to the diffraction pattern. The diffraction pattern of the corresponding aperture function, a sinc-function of scale  $N^{-1}$ , needs to be convolved with our result in eq. 1.15, so that each diffraction order will have this envelope.)

## The Mission

I have given a brief introduction into the importance of lasers in atomic physics, and I have shown in particular how light can act as a potential. Furthermore, I have explained the basics of a quantum gas microscope and the concept of quantum simulation and computation.

The key ingredient of a quantum simulator is the ability to engineer Hamiltonians. This includes the single-site Hamiltonians and interaction terms. The former can be accomplished by creating appropriate potential landscapes by means of laser light. The manipulation of the intensity profile of a laser beam is known as *spatial light modulation*, and that is what this thesis is about. Also, I have shown limitations of optical imaging. Since precision is the key factor in any simulation, aberrations need to be dealt with, and the restricted bandwidth of optical systems needs to be taken into account.

In this work, I will show how a spatial light modulator can be used holographically to measure aberrations in-situ, i.e. in the plane of the atoms, and then create corrected beam profiles of arbitrary shape and project them onto the optical lattice with diffraction-limited performance. The holographic spatial light modulator is a high-precision device that may prove to be valuable in the pursuit of the universal quantum simulator or quantum computer.

## Chapter 2

# Spatial Light Modulation

I have explained the relevance of precise, arbitrary beamshapes for experiments on ultracold atoms in the previous chapter. Now it is time to consider different methods to achieve this goal. Aberration correction and beam shaping can be accomplished using conventional optics, such as wave plates and amplitude masks. These are powerful, but need to be designed and manufactured for each individual situation. Our goal is more ambitious: we are looking for a way to dynamically create arbitrary potentials. In order to reach it, an electronically controllable *spatial light modulator* (SLM) is required.

In the following, I will describe two devices that are commonly used as SLMs, *liquid crystal displays* and *digital micromirror devices*, and explain why the latter is superior for our purposes. After that, I will discuss the placement of the SLM in the image plane and the Fourier plane with their respective pros, cons and resulting application scenarios.

### 2.1 Tools

#### Liquid Crystal Displays

Liquid Crystal Displays (LCDs) are the most common display type today, both for projection and direct viewing, because they are compact, inexpensive and have good optical properties. They consist of a rectangular grid of pixel cells, whose individual transmittance is electrically controlled by modifying the polarization state of the light.

Liquid Crystals are fluids that exhibit an order which resembles structures found in condensed matter physics. Most relevant in display technology is the so-called *nematic phase*, in which prolate molecules are not spatially fixed, but directionally align themselves with each other. The structural reason for this tendency also gives rise to *birefringence*, i.e. an index of refraction of the medium that depends on the polarization vector.

In a *twisted-nematic* LCD, the liquid crystals are set up between two linear polarizers, that are rotated by  $90^\circ$  with respect to each other. The surfaces touching the liquid crystals are structured in a way that aligns close molecules in the direction of the polarizer. Between those surfaces, the nematic character of the liquid aligns the molecules in a helix-structure in order to connect the endpoints smoothly.

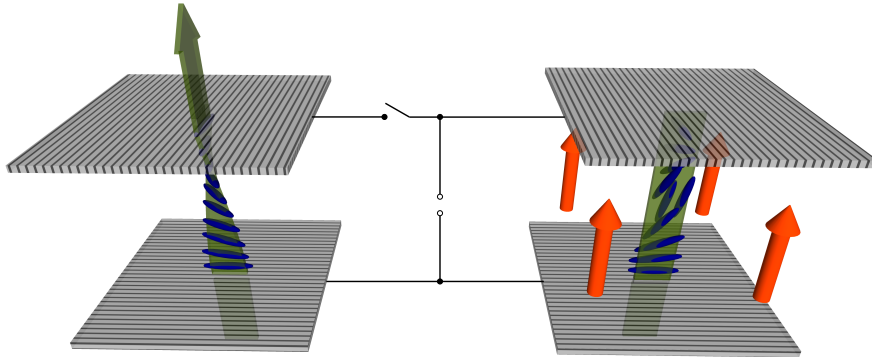


Figure 2.1: A twisted-nematic LC cell with and without applied voltage. An electric field dissolves the natural helix structure of the liquid crystal, reducing the amount of light in the polarization state that can pass through the second polarizer.

Due to circular birefringence, the polarization vector of light passing through the first polarizer will then follow the helix structure and pass through the second polarizer, which acts as an analyzer. Dynamic control of the transmittance is possible by applying electric fields to the crystals. Above a certain threshold, molecules start to align with the external field, breaking the order and dissolving the polarization-rotating chain on the way of the light to the second polarizer. Thus, the rotation of the polarization will be partially or completely suppressed, so that less to no light passes through the analyzer. This is called *twisted-nematic field effect* and illustrated in fig. 2.1. The electronic addressing is usually done by *thin-film transistors* (TFTs).[35]

LCDs have one issue, that make their use in atomic physics problematic. Nematic molecules generally have ionic components, on which the applied voltage acts as a force. This leads to spatial charges that build up quickly, electrolytic degeneration and leakage currents. Instead of DC fields, the field polarization needs to be switched regularly, usually with twice the refresh rate, to prevent this from happening. This makes it impossible to display a truly static image on an LCD. The resulting “blinking”, an oscillation of the transmittance, is invisible for the human eye at sufficient frequencies, but can interfere with atom traps that have depths on a comparable order of magnitude.[36, ch. 5]

In situations where flicker is less critical, LCD SLMs are very useful devices due to their intrinsic grayscale ability (the digital micromirror devices presented in the next section are binary).

### Digital Micromirror Devices

Digital Micromirror Devices are reflective SLMs. They are employed in film theater video projectors and are getting more common in home-use devices as well. Their pixels are tiny mirrors that can be switched individually between two tilt states, so that light is reflected into a particular direction in one state (the “on” state) but into a different direction in the other one (the “off” state). In the following I will specifically describe the *DLP5500* DMD from Texas Instruments that was used in this work, though some of the concepts and properties might

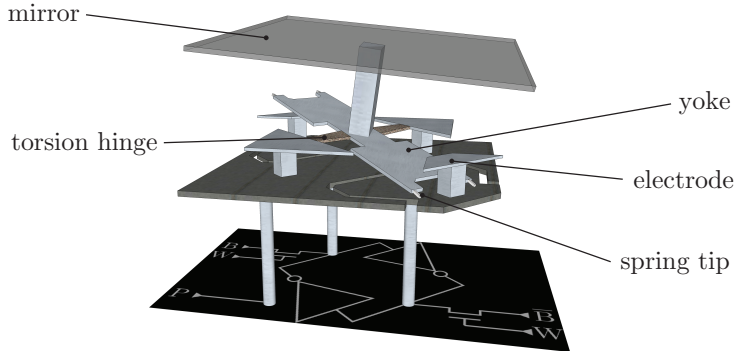


Figure 2.2: Schematics of a single micromirror with control electronics. The electrodes exert a torque on the yoke, which is connected to the mirror and mounted on a torsion hinge. Hard stops at  $\pm 12^\circ$  are enforced by spring tips on the yoke.

be more general than this.

The *DLP5500* is an array of  $1024 \times 768$  square mirrors, each of which is  $10.8 \mu\text{m}$  long. The tilt state is set by electrostatic forces. Each mirror is mounted on a yoke, which is connected to two posts by torsion hinges. Spring tips form hard stops for the yoke at  $\pm 12^\circ$  rotation. The rotation axis is across the diagonal of the mirrors. Electrodes are located along the other diagonal (fig. 2.2, top part).

Each mirror is mounted on top of a CMOS SRAM cell (*complementary metal-oxidesemiconductor, static random-access memory*). Those cells consist of inverter pairs, that are connected back-to-back and keep each other alive.[37, ch. 8] This way, the saved bit B and its complement  $\bar{B}$  can be read out simultaneously. One electrode of the mirror setup is connected to the bit, the other one to its inverse. When a writing signal W is applied, transistors channel the state on the incoming B and  $\bar{B}$  line into the inverter circle (fig. 2.2, bottom part).

In order to reduce the powerthroughput of the SRAM cell, yoke and mirror of all pixel cells share a potential P that is turned on after a new state is written into the SRAM cells. Depending on the bias given by the electrodes this potential will hold the mirrors in the final position.

Extensive studies show that the device still works reliably after one trillion mirror cycles. The hinges do not fatigue and do not get biased over time. Also, mirrors do not get stuck within 100,000 operating hours.[38]

DMDs are available with resolutions up to FullHD ( $1920 \times 1080$ ) and refresh rates up to 23kHz.[39] The fill factor is  $> 90\%$  and the contrast ratio is infinite in principal, since there is no light leakage if all mirrors are turned off. However, due to their binary nature, they do not intrinsically have grayscale capability. Grayscale can be achieved by temporal or spatial averaging. While temporal averaging leads to problems with atom traps, because the refresh rate of the DMD is slower than the timescale defined by the trap frequency, spatial averaging requires a certain number of pixels, so that the effective resolution of the device is reduced by this factor.

Because of the DMD's ability to show truly static images, it is the best choice

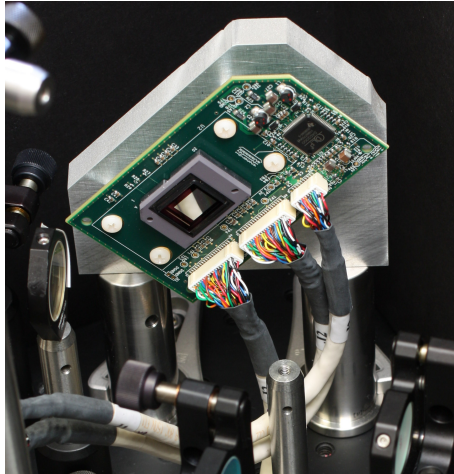


Figure 2.3: DLP5500 DMD mounted in a  $45^\circ$  angle.

for beamshaping in experiments with ultracold atoms. The lack of grayscale capability is a down side, but as I will show later on, high precision beamshaping can be accomplished with binary modulation only.

As mentioned before, the mirrors rotate on a diagonal axis. In order to keep the principal beams in the table plane, we mount DMDs at a  $45^\circ$  angle (see fig. 2.3).

Apart from the mirror chip itself, control hardware is needed to set the state of the memory array and the control bus. The devices that were used in the work described in this thesis are from the *DLP (Digital Light Processing)* series by Texas Instruments. The first device is the discontinued *LightCommander Development Kit*, the second one is of the software-compatible *x3-Series* from the DLP Design House *Keynote Photonics*, both of which use the DLP5500 mirror chip. LightCommander products come with a graphical user interface to display a timed sequence of patterns on the DMD as well as a flexible and powerful C API (*application programming interface*).

## Diffraction

In case of coherent illumination, the individual mirrors act as diffractive elements due to their small size. The two-dimensional mirror array is a reflective grating which means that light is not just reflected into one of two directions, but rather into a number of diffraction orders. The envelope is defined by the diffraction pattern of a single mirror, leading to  $\text{sinc}^2$ -profile with a width of  $\sim 5 - 10^\circ$  for visible and near-infrared light.

For the DMD, the surfaces of that grating are not aligned along the array but at angles of  $\pm 12^\circ$ . The consequence is that the single-mirror-envelope does not line up with the  $0^{\text{th}}$  diffraction order. Illuminating at an angle  $\theta$  the central  $\text{sinc}^2$ -peak is located at  $-\theta \pm 12^\circ$ . Normally we are interested in one particular direction only, so that the distribution of laser power among several diffraction orders is rather inconvenient. The intensity channeled into one order can be maximized by finding the *blazing condition*[40], a common solution to the law

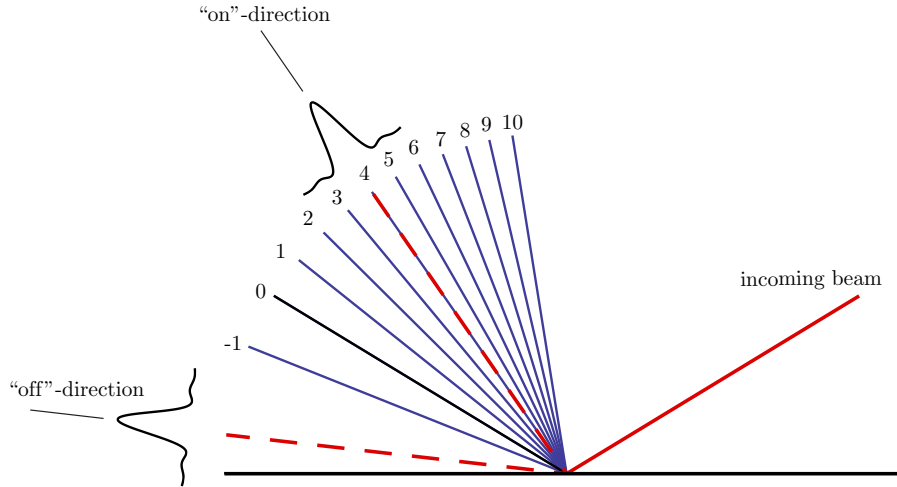


Figure 2.4: DMD geometry optimized for light intensity in the 4<sup>th</sup> diffraction order for a 755 nm laser,  $\pm 12^\circ$  mirror tilt and  $10.8 \mu\text{m}$  mirror size.

of reflection

$$\theta_{\text{in}} = -\theta_{\text{out}} \quad (2.1)$$

and the grating equation

$$d(\sin \theta_{\text{in}} + \sin \theta_{\text{out}}) = m\lambda \quad (2.2)$$

where  $d$  is the spacing of the grating and  $m$  denotes the diffraction order. For the visible light spectrum several solutions can be found that maximize efficiency, one of which is illustrated in fig. 2.4.

I explained earlier that the goal of this work is not only to generate arbitrary beam shapes, but also to cancel aberrations. But how do you get control over the phase profile of a beam when all you have is a binary amplitude mask? The answer is holography.

## 2.2 Amplitude Holograms

We need to be able to make local phase corrections to wavefronts in order to correct for aberrations. Furthermore, we will need to modify the phase profile to create certain higher-order beam modes. Since we are also interested in modifying the intensity profile of the beam, we are looking for a way to locally control both amplitude and phase simultaneously. But how do you modulate the phase with a binary amplitude mask? The solution is holography.

A hologram is a recording of a light field, that allows complete reconstruction of three dimensional objects. Originally, when making a hologram, the coherent light scattered of an object is superimposed with a reference beam. The interference pattern, encoding both amplitude and phase information into a spatial intensity pattern, is imprinted onto a medium. After removing the object, its light field can be recreated with the holographic recording illuminated by the original reference beam. For our purposes we can leave out the recording step

and instead calculate appropriate patterns, that will create a certain light field when illuminated by a coherent source. We can then display those patterns on a spatial light modulator to turn it into a dynamic amplitude hologram.

To understand how this bestowes us the control over phase and amplitude, let us look at a simple example, that is already quite close to what we need. Let us assume we have plane waves illuminating a periodic structure of an opaque material with transparent slits at a non-zero angle. This structure acts as a diffraction grating, so that only certain directions of propagation will have a finite intensity in the far field. These directions are given by the condition, that beams emerging from different slits are in phase (modulo  $2\pi$ ). Stated differently, the condition is that there is a phase gradient of  $0, 2\pi, 4\pi, \dots$  between neighboring slits for the 0<sup>th</sup>, 1<sup>st</sup>, 2<sup>nd</sup>, ... diffraction order, respectively.

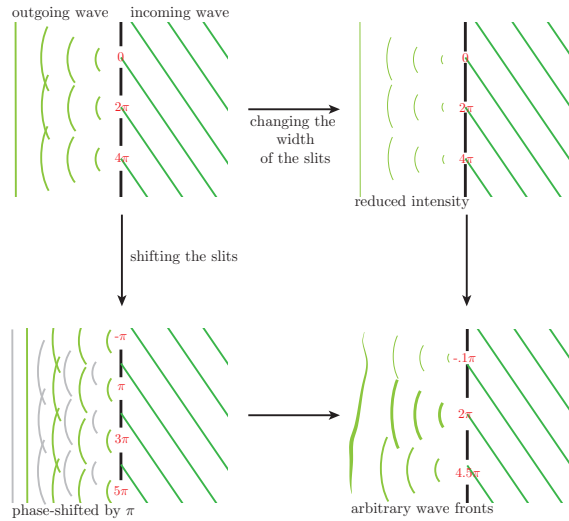


Figure 2.5: Degrees of freedom in an amplitude hologram.

Since there is a linear slope in the phase over the periodic structure, the phase of the outgoing wave can be changed by shifting the slits, or, put differently, changing the phase of the grating. (The grating can be described by a periodic function with a certain spatial phase). Thus, the phase of the diffracted wavefronts is determined by the position of the slits relative to some reference point. Furthermore, the width of the slits determines the intensities of the outgoing beams. Applying those phase and amplitude modifications locally, arbitrary wavefronts can be generated this way. This is illustrated in fig. 2.5.

Apart from this, the direction of beam propagation is given by the periodicity of the grating,

$$\theta_m = \arcsin \left( \frac{m\lambda}{d} - \sin \theta_i \right) \quad (2.3)$$

where  $\theta_i$  and  $\theta_m$  are the angles of the incoming beam and the outgoing beam at the  $m^{\text{th}}$  order, respectively,  $\lambda$  is the laser wavelength and  $d$  is the spacing of the grating. This way the outgoing beam can be steered by modifying the periodicity and, going to a 2D amplitude hologram, the angular orientation of the grating. This is illustrated in fig. 2.6.

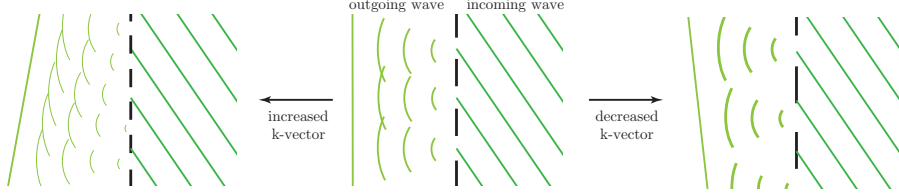


Figure 2.6: Changing the grating's periodicity leads to a change in the direction of propagation, which is governed by the grating equation 2.3

## Light Intensity

An important downside of an amplitude hologram that has to be considered is its low efficiency in laser power. This stems from the distribution of power among several diffraction orders of the grating and the fact, that the opaque parts of the grating cut away parts of the illuminating light field.

As explained earlier, for each diffraction order a complex phasor can be assigned to each point along the grating, representing the complex electric field amplitude at this point. In the 0<sup>th</sup> order, the complex phase and thus the phasor is constant over the period of the grating. In the ±1<sup>st</sup> order, the phase changes linearly by ±2π, in the ±2<sup>nd</sup> order by ±4π.

The amplitude throughput of the grating for each diffraction order depends on the width of the slits. The total outgoing amplitude is the phase-sensitive sum over the light fields along the transparent area. Having a slit of width  $a$  (in units of the period of the grating), the outgoing amplitude is the integral of the phasors over the slit width, from  $-a/2$  to  $a/2$ :

$$A_{\text{out}} = A_{\text{in}} \int_{-a/2}^{a/2} \exp(i2\pi mx) dx \quad (2.4)$$

$$= A_{\text{in}} \frac{1}{i2\pi m} \left( e^{i2\pi m(a/2)} - e^{-i2\pi m(a/2)} \right) \quad (2.5)$$

$$= A_{\text{in}} \frac{1}{\pi m} \sin(\pi ma). \quad (2.6)$$

This leads to an intensity of

$$I_{\text{out}} = I_{\text{in}} \left( \frac{\sin(\pi ma)}{\pi m} \right)^2. \quad (2.7)$$

This is illustrated in fig. 2.7 for the first three positive orders. The first line shows the projection of the local phasor to the real axis, In the second line, phasors corresponding to critical points are printed. Beyond zeroth order, the projected phasor can be positive or negative. Increasing the integration limit will increase the overall amplitude until  $a$  expands into a negative region that leads to partial or complete destructive interference. This is plotted in the third line.

The zeroth order is trivial and not useful for an amplitude hologram - since the phasor is constant, shifting the slits does not tune the phase of the outgoing beam. Since the maximum output intensity is inversely proportional to the

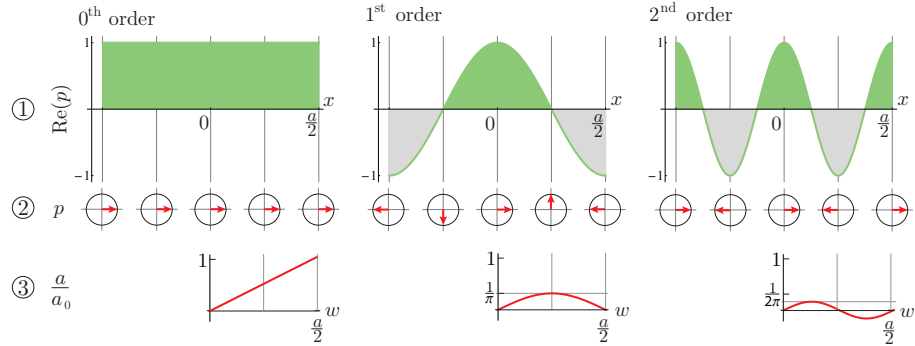


Figure 2.7: Spatially dependent phasor  $p$  of complex light field for different diffraction orders (2) for grating with spacing  $a$ , their projection to the real axis (1), and the scaling of the output amplitude as a function of the slit width  $w$ .

square of the order, the first order yields the best results for our purposes. Its maximum intensity throughput is at  $a = 1/2$ , channeling  $1/\pi^2 \approx 10\%$  into this diffraction order.

## 2.3 Beamshaping

Now that we know what kind of device we want to use, we need to figure out in what context to place it in an optical system. Apart from image planes, another kind of distinguished planes, the Fourier planes, exist, as was explained in chapter 1. These are the two obvious choices for any manipulation on beam profiles, since their effect on the final image plane is readily found. The implications of placing the device in one or the other plane are quite different, however.

The most prominent difference comes from the reciprocal scaling of a Fourier transform,

$$\mathfrak{F}\{g(ax)\}(f_X) = \frac{1}{|a|} G\left(\frac{f_X}{a}\right). \quad (2.8)$$

This means that big features in the Fourier plane correspond to small features in the image plane, and vice versa, in contrast to the direct correspondence for the case of the DMD in an image plane. Apart from holography, a perfect, continuous SLM could perform equally in both scenarios. However, the modulation capability provided by a DMD is both discrete and binary, so that the degrees of freedom of the device are clearly limited. The reciprocal scaling determines how these degrees of freedom, but also the available laser power, are distributed over the image.

### SLM in the Image Plane

When located in an image plane, the DMD mirror states will be directly imaged to the final image plane. This is a conceptually and technically easy way to create arbitrary beam shapes, that are only limited by the discreteness of the device and the optical performance of the imaging system.

If the two mirror states “on” and “off” are not sufficient, a grayscale image can be achieved by averaging over several pixels. Using blocks of  $N$  mirrors,

the formerly discrete step from 0 to  $I_0$  in output intensity is divided into  $N$  equidistant steps. At the same time, the effective resolution of the device goes down by a factor of  $\sqrt{N}$  per direction.

One of the goals of this project, namely the improvement of optical performance by means of holographic aberration control, does not work with the DMD in an image plane. Since imaging systems are linear, the propagation of light from individual pixels can be calculated separately and summed up in the end. But light rays diverging from each of these pixels can take different paths and acquire different phase shifts due to aberrations. This results in a decreased imaging performance. Since the point-spread-function is applied on a single-pixel-level, its shape is not accessible to the DMD in an image plane.

If a high-performance imaging system is at hand, a DMD in an image plane is perfectly suited for projecting big, complex shapes. However, when the goal is to create a sequence of small features at different positions, this is still possible, but strongly limited, for two reasons: First, using few mirrors reduces the amount of control one has over the shape of the beam. And second, the size of the “on”-area is proportional to the output power - thus, dynamically reducing the feature size reduces the output power by the same factor.

### SLM in the Fourier Plane

The scenario is inverted if the DMD is placed in a Fourier plane. This setup is ideally suited for small features, since those have broad Fourier transforms, so that all degrees of freedom can go into the creation of a single small, high-precision shape.

The situation changes when the number of image plane features increases. Every Fourier plane pixel contributes to the intensity at every point in the image plane, so that the more features there are, the more precisely every frequency component needs to be defined. (The total Fourier transform can be imagined as the sum of the Fourier transforms of a number of small image areas.)

Also, big sharp structures in the image plane require high frequency components, so that its Fourier transform needs to be squeezed onto the DMD area. Generally, Fourier transforms converge to 0 for higher frequencies, so that the inclusion of those frequencies means that most pixels are permanently off, reducing the degrees of freedom that can contribute to the beam shape.

Since all frequency components can be addressed individually, an SLM in the Fourier plane can modify the point-spread-function of the total imaging system. By holographic means, both phase and amplitude can be modulated to shape the beam and compensate for aberrations at the same time.

Furthermore, the holographic control makes it possible to create non-trivial phase topologies, such as phase steps or vortices. These are necessary for certain beam shapes such as Laguerre-Gaussian or Hermite-Gaussian beams, which have a wide range of applications in quantum optics.

For those reasons, a holographic DMD, positioned in the Fourier plane of an imaging system, is an interesting and promising beamshaping tool in the pursuit of quantum simulation and quantum computation. I will explain how to use it in order to reduce aberrations of several waves to 1/70th of a wave and create very precise beam shapes in the following chapter.

## Chapter 3

# Holographic Beamshaping

In the first chapter I proposed a way to get local amplitude and phase control over a laser beam by using dynamic amplitude holograms. Those can be provided by digital micromirror devices, as was shown in the second chapter. Assuming all aberrations in the laser path and the intensity profile of the incoming beam are known, this should enable us to cancel aberrations and get diffraction-limited performance, as well as create arbitrary beam shapes. A map of the wavefront distortions and the amplitude profile of a laser beam can be obtained by using the DMD itself. For this, a sequence of amplitude holograms is displayed, and the light intensity is measured by a point detector in the image plane for each hologram. This point detector can be a photo detector behind a pinhole as in my first test setup, or a small, stationary, fluorescent particle like an ultracold atom in an optical lattice, a trapped ion or an NV center.

The advantage and novelty of this approach is that the dectector itself is the object of interest of the experiment (an atom, in our case), that is employed at the position of the experiment (in the lattice). Thus all aberration measurements are performed in-situ. This way no precise manual alignment is necessary since displacement of the focus will show up in the phase map as defocus (longitudinal) and tilt (transverse), and can be corrected easily along with other phase front distortions. The optical system is corrected for imaging errors and fine-tuned in the position of the focus in a single step.

In this chapter I will first explain the general idea of this mapping process, next describe how holograms can be generated and then show results and benchmarks of the aberration control and beam shaping.

### 3.1 Analytical Beam Optimization

In our SLM scheme the DMD that provides the amplitude holograms is placed in the Fourier plane of an optical setup. In the simplest possible case the DMD is illuminated by a collimated beam, and light that is channeled into the  $\pm 1^{\text{st}}$  diffraction order of the amplitude hologram is focused down to the image plane by a single lens (fig. 3.1).

The displaying of a grating over an area that corresponds to the pupil of the imaging system leads to a tight focus in the image plane due to the reciprocity of the Fourier transform (eg. 2.8). The shape of this focus will depend on the amplitude distribution of the beam as well as all aberrations that are present

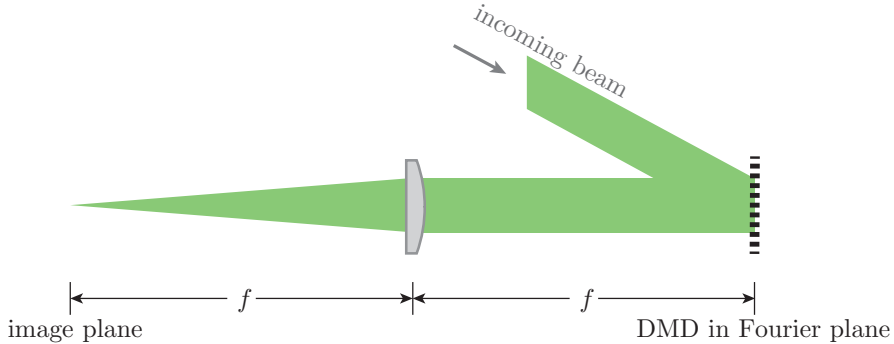


Figure 3.1: Simplified setup: The DMD is illuminated by a collimated beam. The reflected light field is Fourier transformed by a lens and focused to the image plane.

in the system. But these pieces of information are not directly accessible for a point detector in the image plane.

Instead, we can make use of the linear-system character of the setup and try to isolate the system's response to specific frequency components. Frequency components of the image correspond to positions in the Fourier plane, i.e. on the DMD. So the solution is to split the DMD area into a grid of patches and look at each one of those individually.

The propagator of the Fourier spectrum is a frequency-dependent phase factor, as we have seen in the first chapter. If we could measure the phase delay and amplitude for each grid cell, we could assign these values to the corresponding areas on the DMD and use this map for corrections. Since a phase-sensitive intensity measurement is usually not possible, we need to superimpose the beam with a reference beam and extract their relative phase from their interference pattern.

An active patch shows a local amplitude hologram, i.e. a plain grating. Two patches of the grid are active for each measurement: a sampling patch that changes position from one pattern to the next, and a reference patch that is stationary and centered for reasons of noise reduction and convenience (noise adds up if the reference patch is moved, e.g. along-side the sampling patch). This is illustrated in fig. 3.2.

A collimated beam emerges from each of the patches, propagates parallel to the optical axis (ideally on the optical axis in the case of the reference beam) and converges to a small area in the image plane, where the two beams interfere (fig. 3.2). Since absolute phases do not matter in most applications, we define the phase of the reference beam as 0 in the Fourier plane, while that of the sampling beam ( $\Delta\phi$ ) is to be measured.

In a small enough region around the focus, we can describe the beams as two plane waves

$$B_{\text{ref}}(x, z) = a \cdot \exp\left(i \frac{2\pi}{\lambda} z\right) \quad \text{and} \quad (3.1)$$

$$B_{\text{samp}}(x, z) = b \cdot \exp\left(i \frac{2\pi}{\lambda} (\cos \gamma z - \sin \gamma x + \Delta\phi)\right), \quad (3.2)$$

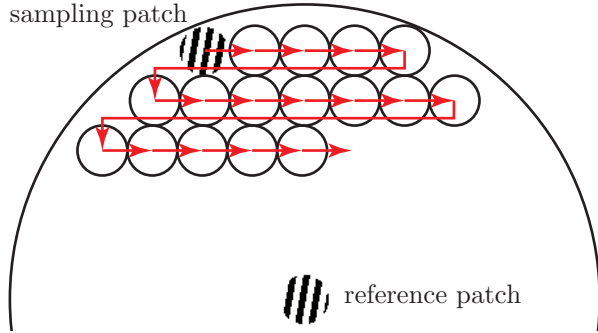


Figure 3.2: Mapping sequence showing the origin of the sampling beam and the reference beam.

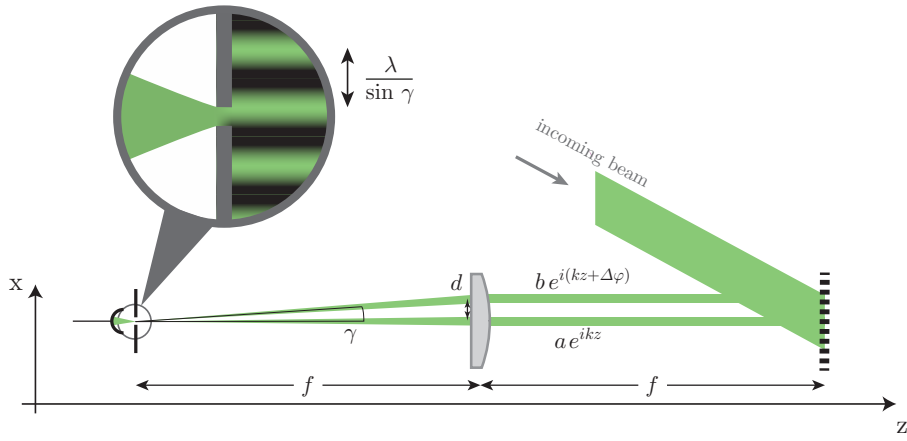


Figure 3.3: A simplified setup: The DMD is illuminated coherently by a collimated beam and the 1<sup>st</sup> diffraction order is focused onto a pinhole with a photodiode behind it.

where  $a, b$  are the amplitudes of the beams and  $\gamma$  is their relative angle defined by the arcus tangent of the distance  $d$  of the two patches devided by the focal length  $f$ . The intensity modulation of the interference pattern becomes

$$|B_{\text{ref}}(x, z) + B_{\text{samp}}(x, z)|^2 = a^2 + b^2 + 2ab \cos \left( \frac{2\pi}{\lambda} ((1 - \cos \gamma)z + \sin \gamma x) + \Delta \phi \right). \quad (3.3)$$

We get interference fringes in the focal plane with periodicity  $\lambda / \sin \gamma$  (fig. 3.3). The interference contrast is proportional to the product of the amplitudes of the two beams, and the phase of the interference stripes is given by the phase difference  $\Delta \phi$  between the beams.

### Retrieving Phase and Amplitude

A single intensity measurement is not sufficient to solve eq. 3.3 for  $\Delta \phi, a$  and  $b$ . More data points along the interference pattern are required to determine

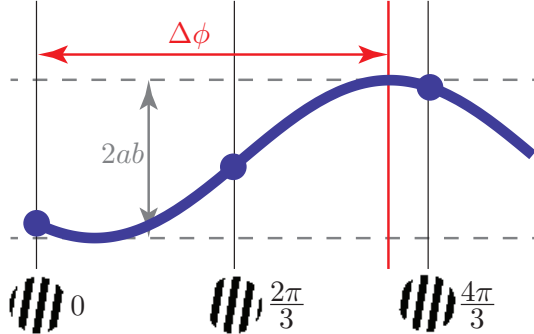


Figure 3.4: Reconstruction of the cosine from three equidistant data points to recover  $\Delta\phi$  and  $a \cdot b$ .

these parameters. It is indeed impossible to specify the amplitudes  $a$  and  $b$ , since interchanging them yields the same interference pattern. Instead, the amplitude of the central beam will be taken as a reference, so that all measured amplitudes will have a factor  $a$  without changing their relative magnitudes. This leaves us with two parameters,  $\Delta\phi$  and  $a \cdot b$ . The former is ambiguous, because the cosine is not single-valued on the interval  $[0, 2\pi)$ . Thus, we need a total of three datapoints to unambiguously determine those parameters.

We are using a stationary point detector, so the only way to scan the interference pattern is to move it relative to the detector instead of the other way round. This can be achieved by shifting the slits of the amplitude hologram that makes up the sampling patch. This will modify the phase of the emerging beam accordingly, as it has been shown in section 1.3.

Most conveniently, the interference pattern can be sampled at three equidistant points along one period (fig. 3.4):

$$m_1 = a^2 + b^2 + 2ab \cos(\Delta\phi) \quad (3.4)$$

$$m_2 = a^2 + b^2 + 2ab \cos(\Delta\phi + 2\pi/3) \quad (3.5)$$

$$m_3 = a^2 + b^2 + 2ab \cos(\Delta\phi + 4\pi/3). \quad (3.6)$$

These data points allow the unambiguous reconstruction of a phasor  $p$  modelling the fringes[41]:

$$p = -\frac{1}{3}(m_2 + m_3 - 2m_1) + \frac{i}{\sqrt{3}}(m_2 - m_3) \quad (3.7)$$

The sought-after numbers are the complex phase and the absolute value of this phasor:

$$\Delta\phi = \arg p \quad (3.8)$$

$$a \cdot b = |p| \quad (3.9)$$

However, depending on the aligning precision and the amount of aberration in the system, the calculated amplitudes may not be reliable. Due to aberrations the focus of different patches can be distinct. Thus their images (Airy disks for circular patches) will not be centered on the image of the reference patch. This

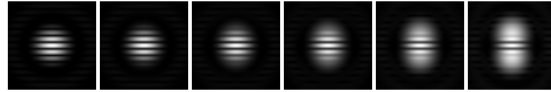


Figure 3.5: Interference contrast of equal-strength Airy disks at different spatial displacements.

mismatch will decrease the interference contrast and - incorrectly - lead to the assumption of a lower amplitude (fig. 3.5).

Running the sequence twice can solve this problem: In the first run, only the phase information is extracted from the measurements. The phase map is applied to generate holograms that compensate for tilt, defocus and higher-order aberrations, so that the foci of all patches will line up perfectly in the second sequence. Now the local amplitudes can be calculated precisely. Also, the second mapping can measure residual wave front distortions to make sure the applied phase map is correct.

## Phase Unwrapping

The aim of this project is to achieve the highest possible flatness of wave fronts. A large number of data points is required for this. We do not have to increase the sampling rate accordingly, though, since we know that aberrations are described by polynomials, and the significant ones are up to order 4 (chapter 1). This allows us to use a much smaller number of measurements and interpolate between them to get good results.

This leads to an issue, because we do not get absolute phases from the measurements. Instead, all phases are projected to the interval  $(-\pi, \pi]$ . It clearly makes a difference for the interpolation if the values of neighboring sampling points are - say -  $(0, \pi)$ ,  $(0, 3\pi)$  or  $(0, -\pi)$ , though the data points are the same mod  $2\pi$ . Thus, correct phase relations between neighboring sampling points need to be found prior to interpolation. This problem is known as *phase unwrapping*.

There exists extensive literature on the topic phase unwrapping, most of which is concerned with topological defects, singularities and noise in situations where the phase changes slowly in space[42]. Our problem is different, since we expect smooth phase profiles, but possibly changes of more than  $2\pi$  between data points, if we want to keep the sampling rate low.

One conceptually easy way to deal with smooth but steep unwrapping is to predict the absolute magnitude of a point based on the slope connecting the two previous ones. Then, multiples of  $2\pi$  can be added or subtracted to the actual measurement to bring the phase as close as possible to the predicted value. This works remarkably well due to the smooth form of aberrations. Fig. 3.6 shows an example measurement of a wrapped phase and the clear path of the gradient-based unwrapping scheme.

This method requires confidence in the actual phase difference of the two measurements that are used as a starting point. If the phase difference is off by multiples of  $2\pi$  here, the resulting phase map will be useless. One possible solution is to oversample locally: in addition to the data points  $(n, y_n)$  and  $(n+1, y_{n+1})$ , one data point in between, say  $(n+1/3, y_{n+1/3})$ , can be acquired. The real phase difference between  $n$  and  $n+1$  can be extrapolated from the

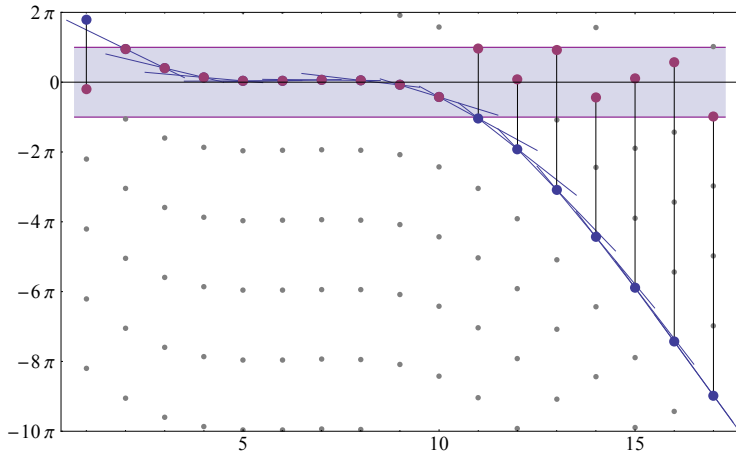


Figure 3.6: Unwrapping based on local slopes: Starting from wrapped phase measurements (pink), the blue spots show the result of the unwrapping sequence that follows gradients to predict the most likely absolute value of the phase.

intermediate point, which is much more likely to be correct. This is illustrated in fig. 3.7a for the 2D case.

At low noise levels, this unwrapping scheme is very robust and does not depend on the chosen path. E.g., after correcting a square of data points as starting point, the phases can be unwrapped following straight lines (fig. 3.7b).

### Hologram Generation

The holograms we use are always based on a one-dimensional grating, which is the binarized version of

$$g(x, y) = \cos(k_x x + k_y y) \quad (3.10)$$

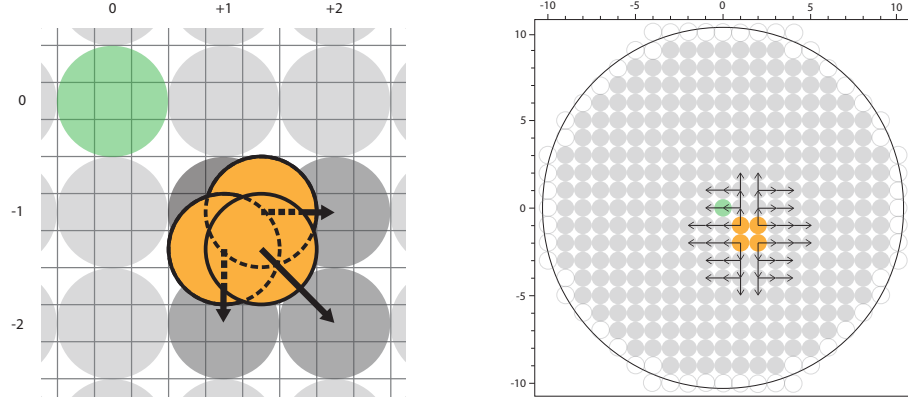
where  $x, y$  are coordinates on the DMD and  $k_x, k_y$  define the k-vector of the grating. The local phase of the grating is given by the argument of the cosine,  $k_x x + k_y y$ . This phase corresponds directly to the phase of the outgoing beam at this point, as has been pointed out in the first chapter. Compensating for aberrations thus is as easy as subtracting the obtained phasemap  $\Delta\phi(x, y)$  from the phase of the grating:

$$g(x, y) = \cos(k_x x + k_y y + \Delta\phi(x, y)) \quad (3.11)$$

For the amplitude modulation, which is the most important part of beam shaping, we start from the map of the local beam amplitudes  $U(x, y)$ . This needs to be compared to the target beam profile  $U_t$ . For each pixel, the ratio between the two,

$$a'(x, y) = \frac{U(x, y)}{U_t(x, y)}, \quad (3.12)$$

is calculated. Since local amplitudes cannot be increased, but only attenuated by the amplitude hologram, the pixel  $(x_l, y_l)$  with the smallest  $a'$  will limit the total intensity of the outgoing beam. In this area, the relative amplitude scaling



(a) To find a flat starting point for unwrapping, a small region is oversampled to correct the absolute value of the nearest neighbors.

(b) The unwrapping sequence is path-independant. Starting with a square of 4 data points, local gradients can be followed to get the absolute values.

Figure 3.7: Getting an unwrapped phase map.

$a$  is set to 1, which corresponds to a slit-width of half the grating spacing. The other parts are scaled down accordingly ( $a(x, y) = a'(x_l, y_l)/a'(x, y)$ ) and their slit-widths are determined by eq. 2.6.

The most straight-forward way to generate the holograms is to assign a slit width  $w(x, y) \in [0, \pi]$  to each pixel in accordance with its amplitude scaling factor, and turn the corresponding mirror on if

$$p(x, y) = |k_x x + k_y y + \Delta\phi(x, y) \bmod 2\pi| \leq w/2 \quad (3.13)$$

or off otherwise. This deterministic approach works, but has two issues:

Firstly, it localizes errors arising from the discrete nature of the device. Fig. 3.8 shows a straight rasterized grating. The black-white transitions show equidistant steps. All those steps combined can form an additional diffractive layer on top of the single-mirror-diffraction and the displayed grating. This is visible in fig. 3.9. The photograph shows an array of spot triplets, where the triplets are the 0<sup>th</sup> and ±1<sup>st</sup> of the grating and the array stems from diffraction orders of the mirror grid. The weaker spots are the result of the deterministic step size in the black-white-transitions. This can be problematic when the main goal is to have strongly localized beams at well-defined positions and the secondary spots are close to the main diffraction order.

Secondly, the binarization is clearly inexact and requires a certain area to approximate a target amplitude value. In certain situations, this approximation converges only slowly, which leads to the formation of artifacts. Especially in regions with low amplitude scaling factor, this can introduce local errors in the Fourier spectrum. In those regions, only a small range of phases will give an “on”-pixel, and it can happen that this particular phase range is statistically underrepresented or overrepresented. This is illustrated in fig. 3.10, where large blank areas appear instead of a smooth decreasing of the amplitude.

In order to circumvent the afore-mentioned problems, a probabilistic approach can be taken. An ideal dithering algorithm would distribute pixels on the

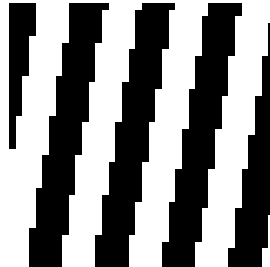


Figure 3.8: Close-up of deterministically generated pattern.

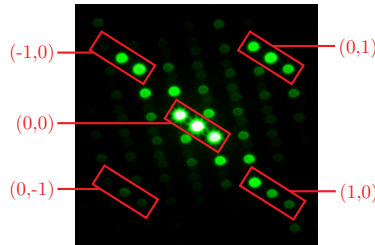


Figure 3.9: Different levels of diffraction orders.

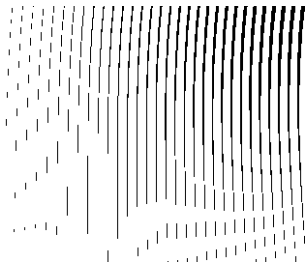


Figure 3.10: Artifacts in the hologram generation lead to local errors.

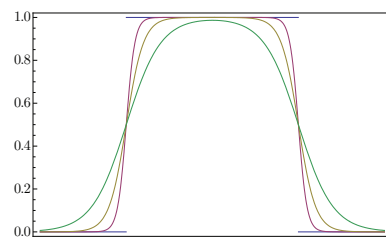


Figure 3.11: Smoothing out the binarization-distribution.

on-off-transition line randomly without effecting the local amplitude throughput and flatten out the phase range of regions with low scaling to prevent artifacts. The deterministic method uses a step function to assign 0 or 1 to a pixel. This can be randomized by smoothing out the distribution, e.g. by using

$$\frac{1}{2} [\tanh(a[p(x, y) + w/2]) - \tanh(a[p(x, y) - w/2])]. \quad (3.14)$$

This is illustrated in fig. 3.11 for different values of  $a$ . The randomized method does not show artifacts and removes the additional diffraction orders by redistributing the noise from the discretization over larger areas. This can be seen in fig. 3.12 for different values of  $a$ .

To get an estimate of the achievable precision with those methods, I simulated a large number of initial conditions and target amplitudes and phases on gratings of different sizes. Fig. 3.13 shows the rms amplitude and phase errors for different grating sizes and spacings. A patch as small as  $5 \times 5$  pixels has an rms error of  $> 10\%$  in defining an amplitude and  $\sim 5\%$  in defining a phase. An

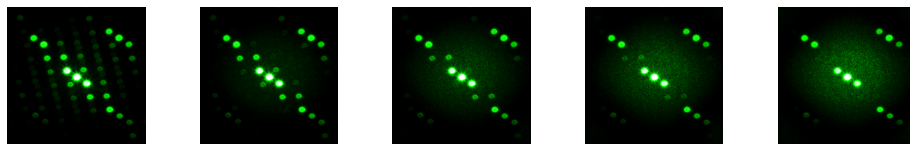


Figure 3.12: Noise modulation for different levels of randomness. The factor  $a$  from eq. 3.14 is decreasing from left to right, leading to a broader probability distribution.

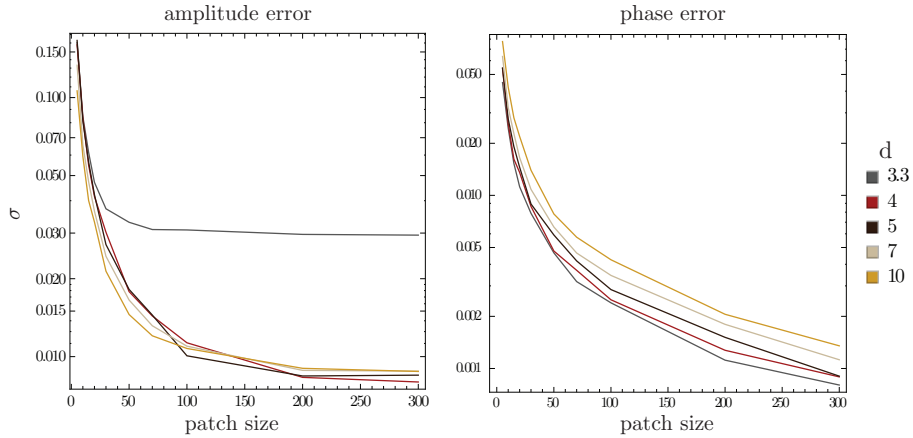


Figure 3.13: rms amplitude and phase errors for gratings of different sizes and spacings.

area of  $100 \times 100$  is required to bring the amplitude error below 1%. This is an important figure of merit. The rms error as a function of the used area defines the actual Fourier space resolution and precision of the holographic SLM.

However, it is questionable if we are fundamentally limited by physics or just by the method we use. Generally, we expect a non-constant phase profile on the DMD area, so that in a certain region, say  $5 \times 5$  mirrors, each pixel should have its unique phase. But that means that  $2^{25} \approx 3 \cdot 10^7$  distinct complex fields can be defined in the image plane, so that the accuracy should be considerably higher than achieved for this area by the previously described method.

On this ground, I tried a brute-force optimization of holograms of that size. Assigning phases to each row according to a k-vector of  $k = 2\pi/5px$  but randomizing the phase relation between the rows and picking a random target amplitude and phase in an imaginary ‘‘image plane’’, I could simulate a wide range of scenarios. I then compared all  $2^{25}$  configurations and used the sum of phase and amplitude deviation from the target value as a merit function. Depending on the application, people do not want to define a Fourier component in one point in the image plane, but have it constant over some finite area. To take this into account, I ran the above simulation for different target sizes in the image plane (fig. 3.14) and used the rms error from  $7 \times 7$  sampling points on this area as merit function. Due to the trial-and-error nature of this calculation, the processing time scales exponentially with the size of the hologram, and is already considerably long for  $5 \times 5$ , so that I had to run the simulation on the *Odyssey* Cluster of the Faculty of Arts and Sciences at Harvard University to get some statistics.

The result is shown in fig. 3.15. Looking at a single point in the image plane, the total deviation from the target values of amplitude and phase is as low as  $10^{-10}$  to  $10^{-8}$  for amplitude scaling factors below 0.5, compared to 10% with the earlier method. The contribution of each pixel to the amplitude is the cosine of the assigned phase. The accuracy in the brute-force attempt is much higher, because positive and negative values are combined to get as close to the desired value as possible, in contrast to the positive-only method described

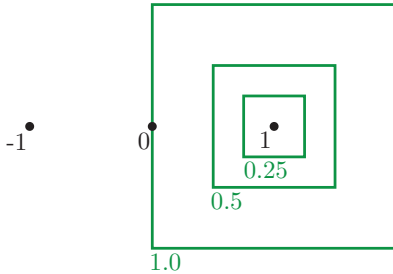


Figure 3.14: Definition of the area factor. The black dots are diffraction orders of the grating. An area around the first order spanning to the zeroth is called 1.

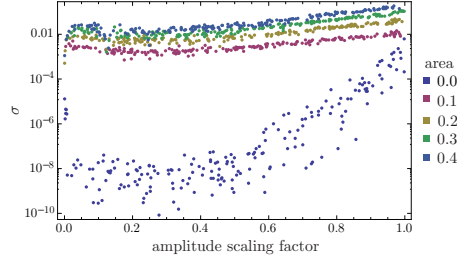


Figure 3.15: Combined amplitude and phase rms error for a  $5 \times 5$  hologram under random conditions, enhanced by brute-force method for constancy over different areas.

before. Large amplitude values have less degrees of freedom, since all large positive pixels have to be used and most negative pixels need to be turned off, so that their generation is more error-prone. The larger the target area in the image plane, the higher the rms error.

Because of the exponential scaling of processing time, it is impossible to enhance full-scale holograms of several  $10^5$  pixels with this method. It should merely act as a “proof of concept”, showing that the hologram generation can be optimized. A probably more feasible way to do it is complex-valued error diffusion[43], which does not necessarily converge to the best solution, but is fast and gives good control over the distribution of noise. No such algorithm was implemented in our system so far. Instead, the randomized distribution method is applied in the following.

## 3.2 First Experimental Results

### Test Setup

In the test setup the DMD is illuminated by a collimated 532nm laser beam at an angle of  $\sim 46^\circ$ . This way, the  $+12^\circ$  tilted mirrors act as a blazed grating for the  $+7^{\text{th}}$  diffraction order at  $-22^\circ$ . The DMD is positioned around the Fourier plane of a 1m lens. In the image plane, a  $10\mu\text{m}$  pinhole is placed in front of a photodiode.

The pinhole size was chosen with respect to the smallest interference period expected for the setup. A quadratic area of  $629 \times 629$  pixels was used on the DMD, where the mapping sequence consisted of  $17 \times 17$  patches with a diameter of 37 pixels. This leads to a maximum distance between parallel beams in the diagonal of about 4.5 mm, resulting in an interference period of

$$d = \frac{\lambda}{\sin \gamma} \approx \frac{532\text{nm}}{4.5\text{mm}/1000\text{mm}} \approx 118\mu\text{m} \quad (3.15)$$

in the image plane. The pinhole size should be considerably smaller than  $d$  to minimize integration over the interference pattern, which reduces the interfe-

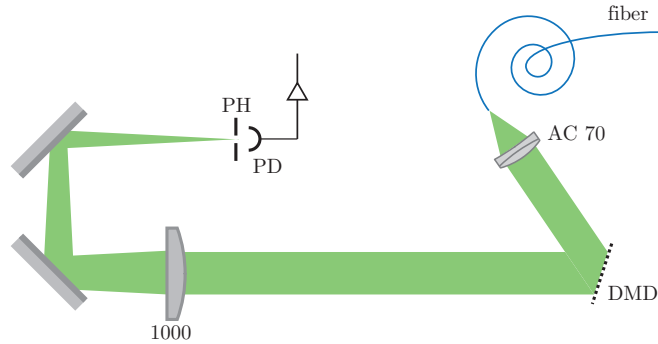


Figure 3.16: Optical test setup: the DMD is illuminated with a coherent, collimated 532 nm beam. The device is positioned in the Fourier plane of a 1 m-lens. The image plane contains a photo diode (PD) behind a pinhole (PH).

ence contrast and will thus falsely appear as decreased amplitude for beams far from the center, where the interference period is smallest.

The photodiode was connected to a *Femto DLPCA-200* low-noise amplifier. A *National Instruments USB-6259 BNC* ADC/DAC was used to measure the resulting voltage and send the data to a computer as well as to trigger the pattern sequence on the DMD.

### Phase Measurement

The mapping sequence was successfully performed in the test setup. Fig. 3.17 depicts the phase map at different processing stages: the sampled data before and after unwrapping and a linearly interpolated profile. It is apparent that strong aberrations are present despite the simplicity of the optical setup. Peak-to-valley distortions of 3 waves ( $6\pi$ ) are visible.

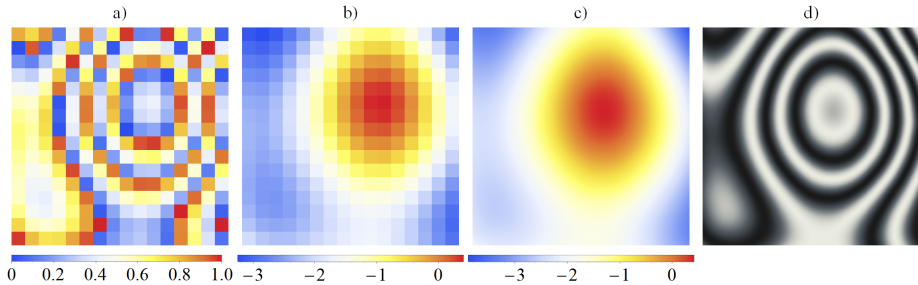


Figure 3.17: Phase maps: a) wrapped, b) unwrapped, c) interpolated, d) corresponding interferometric image ( $\sin(\Delta\phi)$ ). Scales in units of  $\lambda$ .

The major part of those distortions is caused by the mirror array itself. This is due to the mounting process: the DMD chip is pressed onto a heat sink to increase durability, but this leads to a bending of the surface.[44] This is not

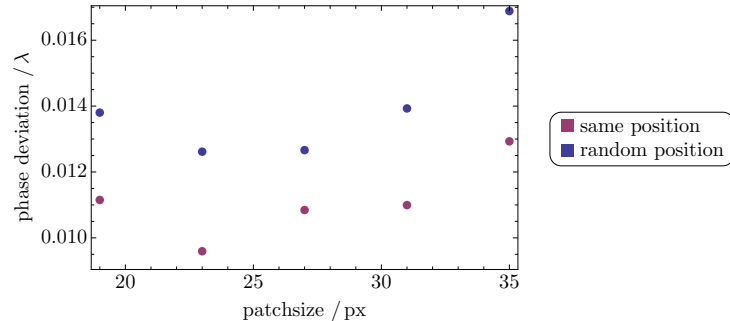


Figure 3.18: RMS phase error after applying corrections for different patch sizes. The figure shows data for measuring on the original grid (purple) and on random positions (blue).

highly problematic, since the holographic SLM can correct any aberrations in the optical system, including those induced by itself.

Repeating the phase measurement with corrections applied show an rms phase error (*root mean square*) of about 1% of a wave. The capability of the DMD to define a precise phase is limited by its discrete and binary nature. Fig. 3.18 relates this rms error to the diameter of the patches in the calibration sequence (purple). It also shows the phase deviation for sampling the corrected wave front at random positions rather than the positions on the grid that were already used for the original measurement (blue). Generally, smaller patch sizes give fewer pixels to define a precise phase, but also introduce less error from integration over finite areas and interpolation, which leads to the rising phase errors for larger patches. The 0.3% higher phase error for random sampling is solely due to the interpolation. A diameter of 23 pixels seems to be the best compromise between phase-defining capability and averaging, though the residual phase error of larger patches is still negligible in practically all situations.

## Amplitude Measurement

The amplitude measurement revealed an illuminating beam profile that is close to a Gaussian. The obtained amplitude map is plotted in fig. 3.19. Repeated measurements yield an RMS error of the data of 0.2%.

## Beam Profiling

In order to see the effect of the phase and amplitude modifications on the image, we need a way to measure the intensity profile of the beam. This is typically accomplished by a CCD camera. We do not depend on such a device, since the holographic DMD can steer the beam. Instead, the beam is scanned over the pinhole that is already in place. This way, crosssections or 2D profiles can be measured with the setup at hand.

According to chapter 1.2, a tilt in the phase profile changes the location of the focus in the image plane. A tilt is a linear phase slope

$$\Delta\phi(x, y) = \Delta_x x + \Delta_y y \quad (3.16)$$

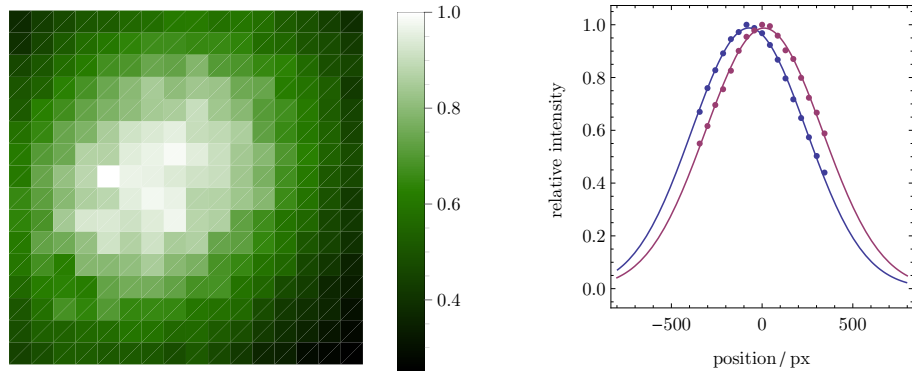


Figure 3.19: Measured amplitude map. The figure on the right shows crosssections integrated horizontally and vertically with Gaussian fits.

and thus corresponds to changing the  $\mathbf{k}$ -vector that generates the grating (cf. eq. 3.11):

$$p(x, y) = \cos(k_x x + k_y y + \Delta\phi(x, y)) = \cos((k_x + \Delta_x)x + (k_y + \Delta_y)y) \quad (3.17)$$

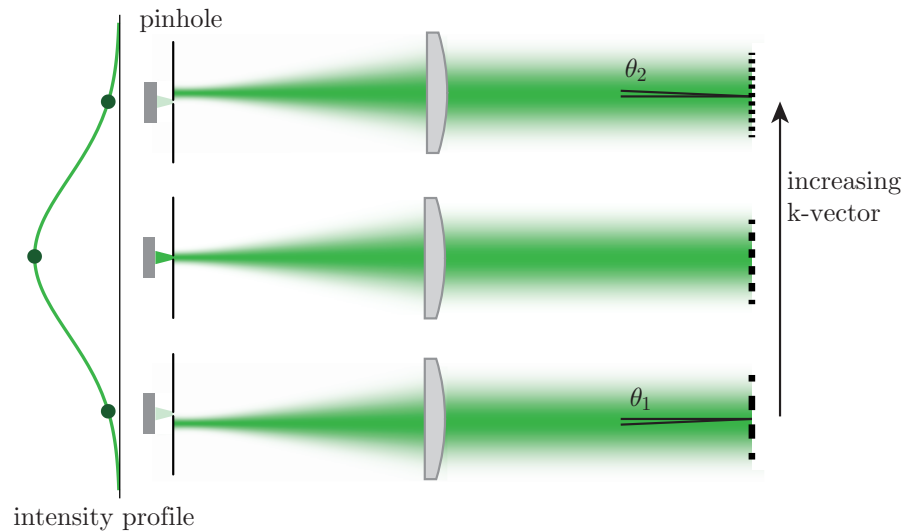


Figure 3.20: Beam profiling can be accomplished by scanning the beam over a pinhole.

The scale of the scanned profile can be calculated from the grating equation

(eq. 2.3). Simplified to 1D, it yields a difference in the propagation angle of

$$\begin{aligned}
 \Delta\theta &= \theta_2 - \theta_1 \\
 &= \arcsin\left(\frac{\lambda}{d_2}\right) - \arcsin\left(\frac{\lambda}{d_1}\right) \\
 &= \arcsin\left(\frac{\lambda k_2}{2\pi}\right) - \arcsin\left(\frac{\lambda k_1}{2\pi}\right) \\
 &\approx \frac{\lambda \Delta k}{2\pi}
 \end{aligned} \tag{3.18}$$

for the first diffraction order, where  $d_{1,2}$  is the grating period at the two extremal positions and  $k_{1,2}$  the corresponding k-vector (fig. 3.20).

The scanning resolution can be very high with angular steps of  $10^{-6}$  rad or lower. This also sets the upper limit for steering precision. With the long lens in the test setup, this translates to  $< 1 \mu\text{m}$ . Making the transition to high numerical apertures, beams can be positioned with precision on the nanometer scale.

## Gaussian Beam

The Helmholtz equation yields a complete set of free-space propagation modes. The lowest order solution is the Gaussian beam,  $\text{TEM}_{00}$  for *transverse electromagnetic* (0, 0) mode, that has already been mentioned before. It is particularly important in laser physics, because it is the most natural transverse laser mode.

This is why it will be the first test subject for aberration control and beam shaping. The illuminating light has almost, but not quite the right profile. Also, the aberrations that are present in the system blow up the focus.

Fig. 3.21 a-c illustrates the effect of the aberration compensation and amplitude modulation on the hologram: former straight grating lines bend and their widths decrease towards the edges to give rise to a correctly-shaped and aberration-free Gaussian beam. A collimated Gaussian beam of diameter  $d_0$ , that is focused by a lens with focal lens  $f$  should have a spot size of [45, ch. 17]

$$d \approx \frac{2f\lambda}{d_0} \tag{3.19}$$

in the image plane. The diameter of a Gaussian beam is the diameter at  $e^{-2} \approx 14\%$ . With  $\lambda = 0.532 \mu\text{m}$ ,  $f = 1000 \text{ mm}$  and  $d_0 = 3 \text{ mm}$  we expect a spot size of  $d = 0.355 \mu\text{m}$ .

The measured cross section of a beam with and without corrections is plotted in fig. 3.21d. Starting with  $3\lambda$  aberrations, there is severe destructive interference in the image plane, which leads to an ill-shaped, blurred spot. The plot includes a linear and a logarithmic scale to fully appreciate the high quality of the correction: the enhanced beam profile resembles a Gaussian perfectly to at least four orders of magnitude. The wings are suppressed to the noise level of the photodiode and the amplifier at  $10^{-4}$  peak intensity. Also plotted is a fit with the a-priori estimate of the width, which matches the measurement extremely well.

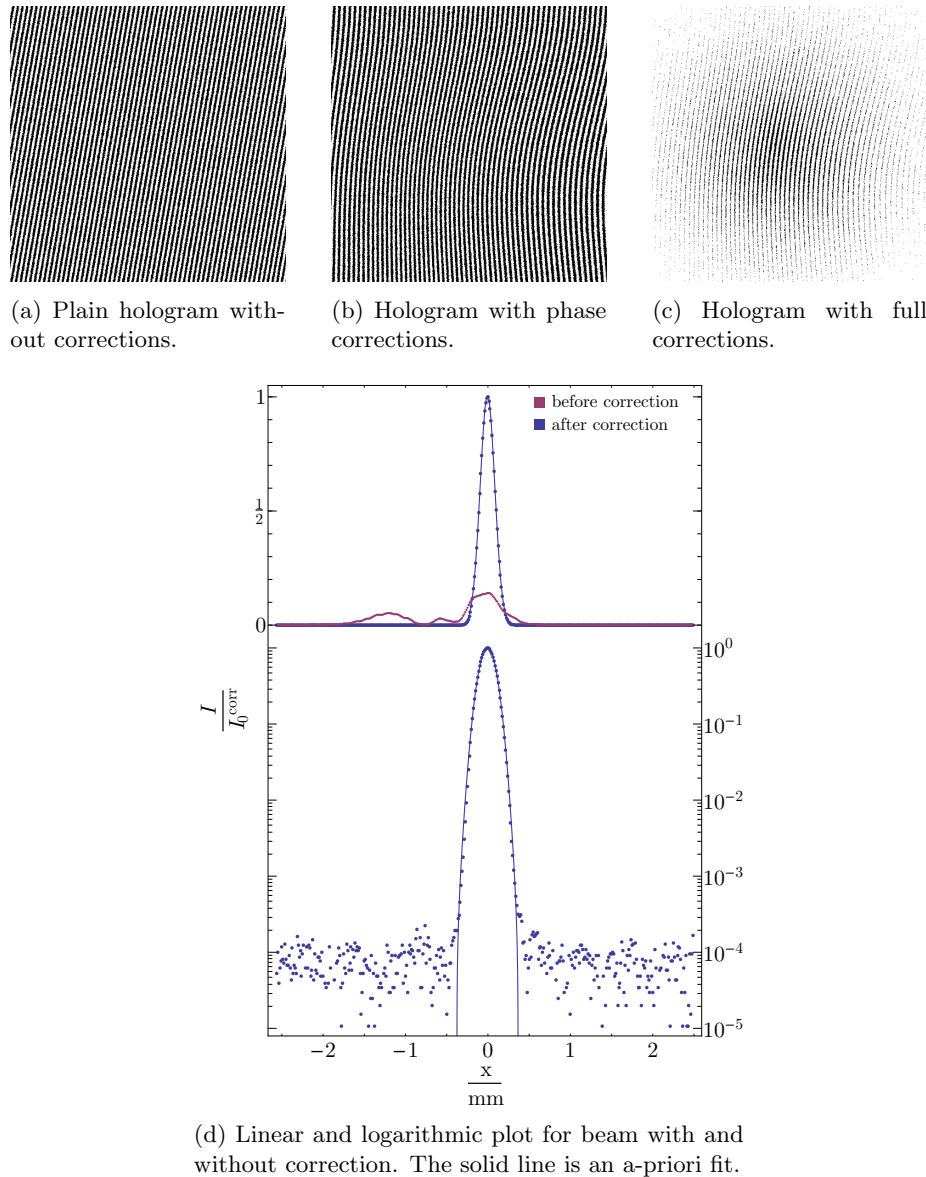


Figure 3.21: Generation of a Gaussian beam.

### 3.3 Advanced Beamshaping

I have shown how to flatten wave fronts and modify the amplitude profile of a beam. Some beam shapes, however, require non-flat phase fronts. The necessity for phase modifications and applications will be discussed in this section.

Our goal is to produce certain intensity distributions in the image plane, where phases are usually not of any interest. But the Fourier transform of the amplitude distribution  $U$ , which determines the required pattern on the DMD, is generally a function  $\mathfrak{F}(U) : \mathbb{R}^2 \rightarrow \mathbb{C}^2$ . Complex phasors can be realized with a hologram by setting the slit width according to its absolute value and the slit position according to its phase.

There are many cases where the Fourier transform is a real function, though. A particularly important subset of those are symmetric functions. Splitting a one-dimensional, real function  $f(x) = f_e(x) + f_o(x)$  into odd and even parts and using Euler's formula  $\exp(iy) = \cos y + i \sin y$ , we get the Fourier transform

$$\begin{aligned}\mathfrak{F}\{f\}(k) &= \frac{1}{\sqrt{2\pi}} \int_{\mathbb{R}} f(x) \exp(ikx) \, dx \\ &= \frac{1}{\sqrt{2\pi}} \int_{\mathbb{R}} [f_e(x) + f_o(x)] \cdot [\cos(kx) + i \sin(kx)] \, dx \\ &= \frac{1}{\sqrt{2\pi}} \left[ \int_{\mathbb{R}} f_e(x) \cos(kx) \, dx + i \int_{\mathbb{R}} f_e(x) \sin(kx) \, dx \right. \\ &\quad \left. + \int_{\mathbb{R}} f_o(x) \cos(kx) \, dx + i \int_{\mathbb{R}} f_o(x) \sin(kx) \, dx \right].\end{aligned}\quad (3.20)$$

But the integral of an odd function over  $\mathbb{R}$  is zero, so that the second and third term drop out, leaving us with

$$\mathfrak{F}\{f\}(k) = \frac{1}{\sqrt{2\pi}} \left[ \int_{\mathbb{R}} f_e(x) \cos(kx) \, dx + i \int_{\mathbb{R}} f_o(x) \sin(kx) \, dx \right].\quad (3.21)$$

Thus, the Fourier transform of an even function ( $f_o(x) = 0$ ) or and odd function ( $f_e(x) = 0$ ) is real (dropping the  $i$  in front of the second term, which is a negligible overall phase factor). Most beam profiles that are considered in the following are symmetric, i.e. either even or odd, so that a real-valued amplitude distribution is required in the DMD plane in those cases.

Those function's codomain is not limited to  $\mathbb{R}^+$  though - negative values occur frequently and need to be accounted for on the DMD. Other groups solved this by redefining zero to a "gray" level at 50% amplitude transmittance, so that no light and full light correspond to minus maximum amplitude and plus maximum amplitude, respectively ([17]). The down-side of this approach is the reduction of dynamic range in amplitude modulation by a factor of 2 and a background signal in the image plane. The better solution is to account for negative values by a phase factor  $\exp(i\pi) = -1$  on the phase map. This way the dynamic range is preserved and no features are added in the image plane.

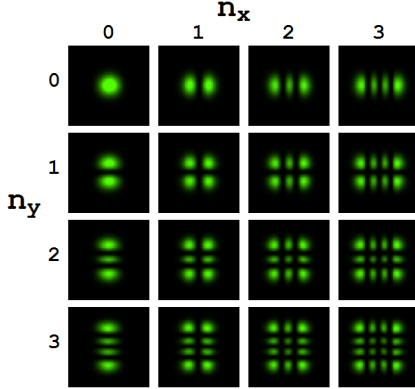


Figure 3.22: 2D scans of Hermite-Gaussian beam profiles in different orders.

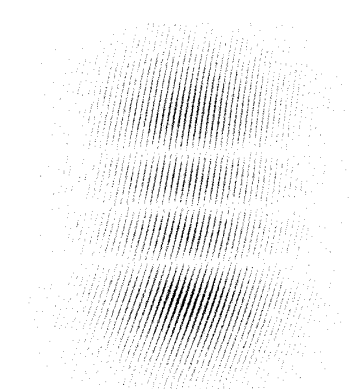


Figure 3.23: Hologram for a  $\text{TEM}_{03}$ .

Figure 3.24: Hermite-Gaussian beams.

### Hermite-Gaussian Beams

The Hermite-Gaussian beams of order  $(m, n)$ , commonly called  $\text{TEM}_{mn}$  modes, are defined as

$$\text{TEM}_{mn}(\vec{r}) = \text{H}_m\left(\sqrt{2}\frac{x}{w}\right) \text{H}_n\left(\sqrt{2}\frac{y}{w}\right) e^{-\frac{x^2+y^2}{w^2}} \quad (3.22)$$

where  $w$  is a free parameter and  $\text{H}_j(x)$  stands for the Hermite polynomial of order  $j$  in  $x$ . They are Fourier-invariant free-space modes.

The first few orders of Hermite-Gaussian amplitude profiles and measurements are depicted in fig. 3.22. As explained before, at each zero-crossing of the Hermite polynomials a  $\pi$ -step is added to the phase map in order to account for negative parts. The resulting pattern for a  $\text{TEM}_{03}$  is shown in fig. 3.23.

### Laguerre-Gaussian beams

Laguerre-Gaussian beams are higher-order transverse free-space modes defined by

$$\text{LG}_p^l(\vec{r}) \propto r^{|l|} \text{L}_p^l\left(2\frac{r^2}{w^2}\right) e^{-\frac{r^2}{w^2}} e^{il\phi} \quad (3.23)$$

where  $\text{L}_p^l(x)$  are generalized Laguerre polynomials and  $w$  is a free parameter. The circularly symmetric profile has  $p$  radial nodes  $x_n \neq 0$ . The term  $r^{|l|} e^{il\phi}$  gives rise to a central node and phase vortex of order  $|l|$ . This mode is Fourier-invariant, too.

In the generation of holograms, the circular phase  $l\phi$  needs to be added to the local phase of the grating given by  $k_x x + k_y y + \Delta(x, y)$ , leading to a branch cut in the phase map. The effect is an  $l$ -fold branching of the central slit, as illustrated in fig. 3.25.

The phase vortex has two interesting consequences. First, it leads to an angular momentum carried by the beam. Second and more importantly for our

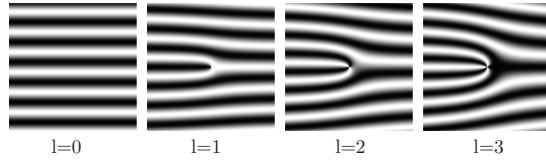


Figure 3.25: Amplitude hologram for different orders of vorticity.

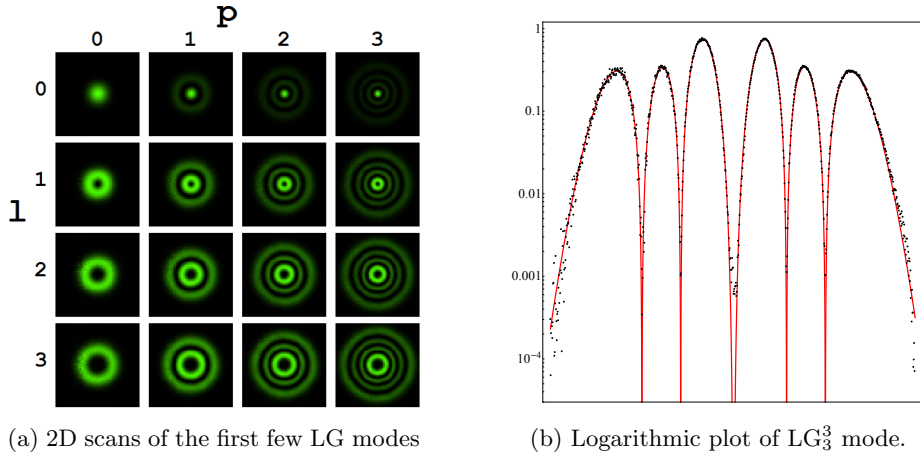


Figure 3.26: Measurements of Laguerre-Gaussian beams.

purposes, it *topologically enforces* the central node, because the amplitude profile is circularly symmetric, so that for each point there is a point with the same absolute value but different sign in the Fourier plane, which leads to destructive interference in the center of the focus in the image plane. This point is opposite for  $l = 1$ , and generally  $\pi/l$  ahead in  $\phi$ .

The central node is the most significant feature of Laguerre-Gaussian beams in atomic physics, because they are used with blue-detuned lasers to trap atoms in the central minimum. It is crucial in many applications that this minimum is at absolute zero (REF), so that no additional potential is acting on the atoms.

Measurement results are shown in fig. 3.26. It depicts two-dimensional scans of the Laguerre-Gaussian modes  $l = 0..3$  and  $p = 0..3$  alongside a logarithmic plot of the crosssection of the  $LG_3^3$  mode, which shows excellent agreement with the target profile (red). Particularly promising is the value of the minimum below  $10^{-3}$  rim intensity. This number is rather an upper limit than the actual value, since the intensity is scanned with a  $10\ \mu m$  pinhole which integrates the intensity over a finite area, and the crosssection can be slightly decentred. The actual intensity in the center can thus be expected to be considerably lower.

## Flat Top

In most optical lattice experiments, atoms are constrained to a small area on the lattice by a dipole trap, i.e. a red-detuned beam, or a blue-detuned LG beam (“donut”). In either case, atoms are subject to a harmonic confinement in second order approximation. This is necessary to keep the atoms together in

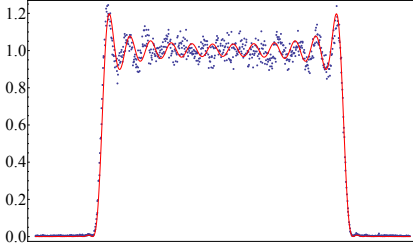


Figure 3.27: Measurement of a box potential. The solid red line is a simulation for a smooth, non-binary hologram.

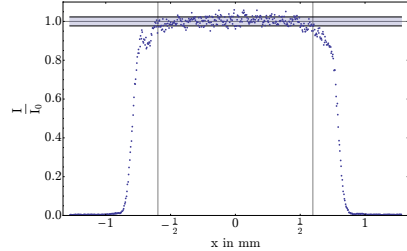


Figure 3.28: Smoothened flat-top beam.

the superfluid phase, in which the trap depth of the lattice is low and tunneling occurs at a high rate ([22]).

However, the harmonic confinement is a spatially-dependent potential. It changes the local chemical potential and thus the dynamics of the system. Clearly, it would be better to have a box potential, i.e. a flat bottom and steep walls to trap the atoms, so that their behavior is unchanged. Such a *flat-top* potential can be generated by an SLM.

With this, we are leaving the realm of Fourier-invariant functions, and this is where things are getting a little more messy. The problem lies in the limited dynamic range of the holographic DMD. It is easy to flatten the beam profile in the Fourier plane and cut off the intensity beyond a certain region. To create this profile in the image plane, however, the Fourier transform of a box - a sinc function - needs to be displayed. The problem with infinitely sharp edges is that their Fourier transform converges slowly. Very high frequency components are needed, but their amplitudes quickly drop below the amplitude resolution of our devices.

The result is a frequency cut-off, that not only leads to reduced steepness, but also to the occurrence of visible ripples on the top. The scanned profile of an attempted box-shaped beam is plotted in fig. 3.27. It is quite useless for the application of a flat trapping potential.

Alternatively, the ripples can be traded-off against steepness. The idea is to choose a smooth profile that is relatively flat on top and has relatively steep edges.

Alternatively, the ripples can be traded-off against steepness. The idea is to choose a smooth profile that is relatively flat on top and has relatively steep edges. For example, this can be achieved by the expression

$$f(x) = \frac{1}{\pi} (\arctan(ax + b) - \arctan(ax - b)). \quad (3.24)$$

The Fourier transform of arctan is known to be

$$\mathfrak{F}\{\arctan(x)\} = i \sqrt{\frac{\pi}{2}} \frac{e^{-|k|}}{k} \quad (3.25)$$

Using linearity and symmetries of the Fourier transform

$$\mathfrak{F}\{g(ax)\} = \frac{1}{|a|} G\left(\frac{k}{a}\right) \quad (3.26)$$

$$\mathfrak{F}\{g(x+a)\} = G(k)e^{i2\pi ka} \quad (3.27)$$

where  $\mathcal{F}\{g(x)\} = G(k)$ , we get

$$\mathfrak{F}f(x) = \frac{\sqrt{2\pi}}{k} \exp\left(-\frac{|k|}{a}\right) \sin(bk). \quad (3.28)$$

A beam profile created this way is plotted in fig. 3.28. The achieved rms flatness in the central region is  $\sigma = 2.3\%$ . The size of this region depends on the optics used and can be scaled within a huge range of values from few  $\mu\text{m}$  to several mm.

### The Limits of Complexity

To test the limits of the system I left the domain of analytic expressions and tried numerical Fourier transforms of more complex shapes to figure out how arbitrary the beamshapes can actually be.

The procedure here is analogous to the analytical case: First, the Fourier transform is calculated, scaled and cropped to fit the DMD area. Next, the complex phase of the Fourier transform is added to the measured phase map, and an amplitude scaling map is generated from the measured profile of the illuminating beam and the absolute values of the Fourier transform. Holograms are calculated based on those two data arrays.

Fig. 3.29 shows scans of more complex shapes created this way, from institutions involved in atomic physics as well as from popular culture.



Figure 3.29: Measured beam profiles based on numerical Fourier transforms.

Generally, there is a trade-off between feature sharpness and stability of the intensity distribution. This has already been observed with the generation of the flattop beam: there, the sharp edges were removed to improve the noise level on the flat surface. Here, this matters in the choice of the cutoff frequency in the Fourier spectrum when scaling it to the DMD area. Including higher components gives sharper features and details. But Fourier components generally

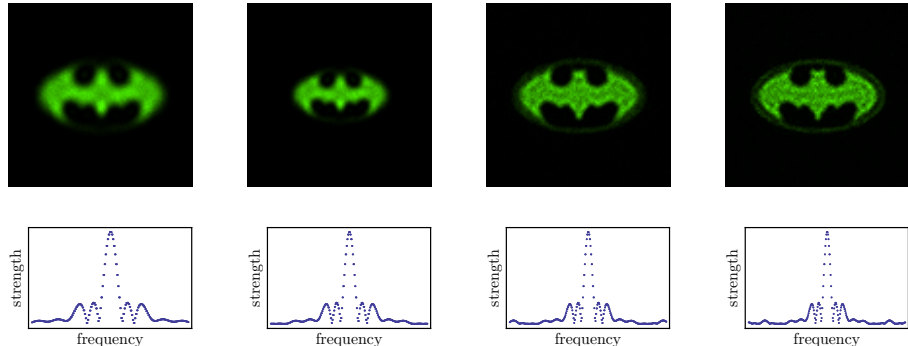


Figure 3.30: Measured beam profiles for different cutoff frequencies in the Fourier plane, increasing from the left to the right. Inclusion of higher frequencies enhances feature details, but also increases the noise frequency. The top row shows the measured 2D beam profiles, the bottom one features a cross section of the respective frequency spectrum.

approach zero for higher frequencies, so that scaling the Fourier transform to include those high frequencies results in an increasing number of pixels that are permanently off. This means that their degree of freedom does not contribute to the shaping precision any more, and the total flatness is decreased. This is illustrated in fig. 3.30.

The actual rms noise does not change for the different parameters here, but is around 18% in all four cases. The noise frequency, however, increases with the inclusion of higher Fourier components. Also, the total intensity goes down by 93% from the left to the right as a consequence of Fourier space compression.

## Chapter 4

# High-NA Applications

### 4.1 Preliminary Considerations

In order to resolve small structures like atoms in optical lattices, objectives with high numerical aperture are required. By definition, these violate the paraxial approximation that is so commonly used in optics. In particular, front and back focal planes of a high-NA lens are no longer exact Fourier transforms of each other, so that the diffraction by the lens aperture has to be reconsidered. Furthermore, polarization issues arise from beams converging from a wide range of angles.

As I have shown in the first chapter, the Fourier transforming property of lenses emerges in the small-angle approximation. The correct image corresponding to a certain field distribution in the “Fourier” plane can be obtained numerically for larger angles. One way to do this is to assign a quadratic phase profile to some amplitude distribution to emulate the effect of a focussing lens. The field at any point in the image plane is the phase-correct integral of all phasors over the aperture, taking path differences to this point into account.

Fig. 4.1a illustrates the effect on the beam shape from switching from low to high NA situations by comparing an exact Fourier transform of a Gaussian beam with a diffracted Gaussian beam at NA 0.7. The latter shows side lobes of 2.2% central intensity instead of exponential decay.

The other new aspect at high numerical apertures stems from polarized interference at high angles. Assuming linearly polarized (in y-direction, say), collimated illumination of a short lens, the light rays bent by the glass will keep their polarization *in their own reference frame*. That means, the vectors of their electrical fields will have a component in the y-direction as well as the longitudinal z-direction. In this *vectorial light field*, the distinct components will interfere individually.

If the phase profile is flat and the beam shape symmetric, the longitudinal components will cancel out and the sole impact is an amplitude modulation from the cosine-term of the projection of the polarization vector to the image plane. While this effect is tolerable for Gaussian beams, the ramifications for topologically created field minima like Hermite or Laguerre Gaussian beams can be much worse: when opposite parts of the beam are phase-shifted by an odd number of  $\pi$ , the longitudinal components add constructively, resulting in a finite intensity where the field is supposed - and possibly required - to be zero

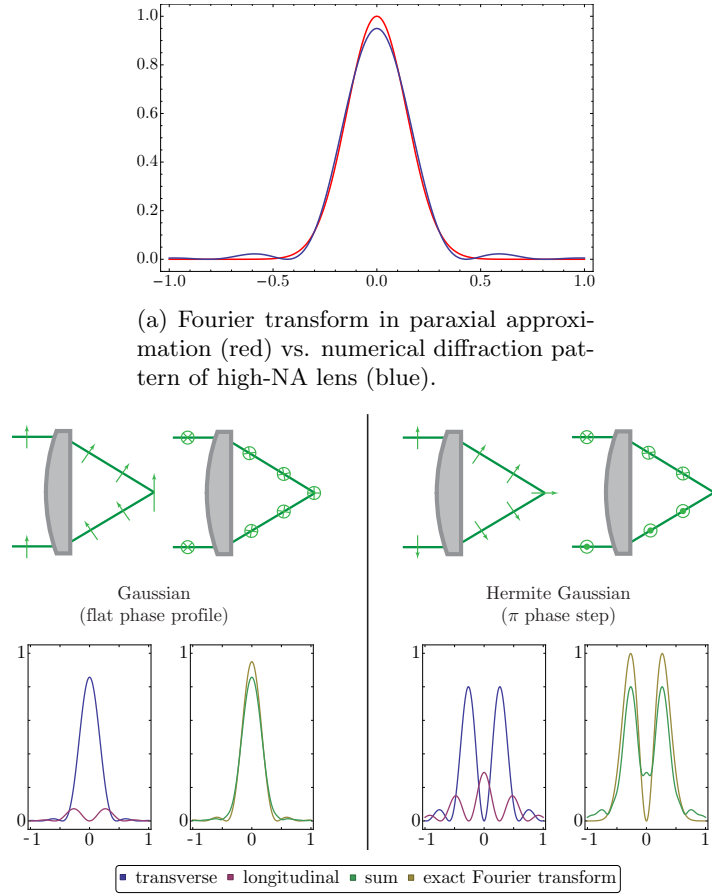


Figure 4.1: The Fourier transforming property of lenses is a paraxial approximation. It fails for high numerical apertures.

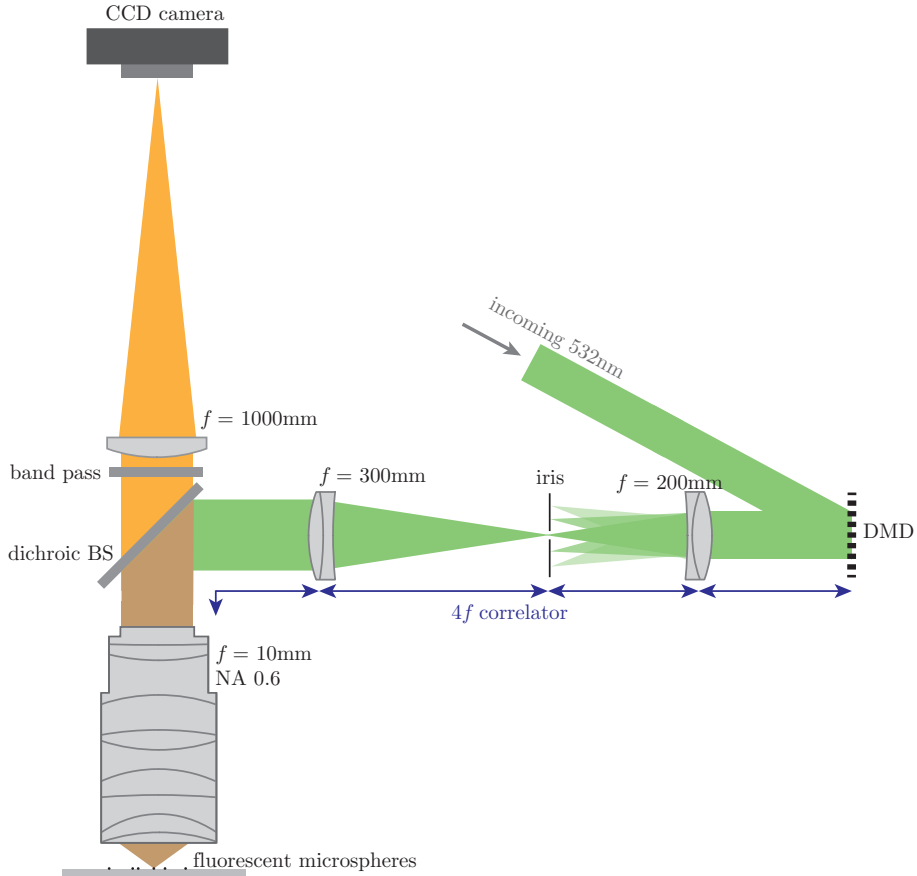


Figure 4.2: Optical setup for microsphere experiment. The dye is chosen for excitation with green light and emission in orange. A dichroic beam splitter combined with a band pass filter separate the paths of the laser light and the fluorescent light. The latter is captured by a CCD camera.

(fig. 4.1b). Thus, only phase singularities of *even* order should be used in those cases.

## 4.2 Fluorescent Microspheres

As a “proof of concept” for the beamshaping and correction scheme in a high-NA situation, I built a second test setup, in which stationary, fluorescent microspheres were used to simulate trapped atoms. The *FluoSpheres®* from *Life Technologies* are beads formed out of polystyrene and are loaded with highly fluorescent dyes.

The microspheres are delivered as colloids in an alcoholic suspension. Since the experiment requires stationary particles, these need to be dried onto a surface. The polymers are available with different surface modifications so that their coupling with other molecules can be changed. A carboxylate-rich surface carries a negative charge. By treating a glass slide with *Polydiallyldimethylam-*

*monium chloride (PDDA)*, its surface accumulates positive charges. When the suspension comes in contact with the treated glass slide, the carboxyl groups bond with the positive charges and glue the microspheres onto the glass. Careful rinsing removes the fluid and additional colloids, leaving a number of stationary, fluorescent beads on the glass surface.[46]

The chosen specifications of the microspheres are a colloid size of 100 nm, an excitation spectrum peaked around 540 nm (green) and emission spectrum around 560 nm (orange).

In the optical setup, the DMD is positioned in a Fourier plane and illuminated with a collimated 532 nm laser beam. The +1<sup>st</sup> diffraction order is selected by an iris in an intermediate image plane. This plane is then Fourier transformed to the back focal plane of an NA 0.6 objective ( $f = 10$ ). The microspheres sit on a glass slide in its front focal plane. Before reaching the objective, the laser beam passes through a dichroic beamsplitter with a cutoff at 540 nm. Fluorescent light from the microspheres is collected by the objective and is passed into a different direction by the beam splitter. After cleaning up the spectrum with a band pass filter, the orange light is focused onto an *Apogee Alta U260* CCD camera (*charge-coupled device*) by an  $f = 1000$  lens. This imaging yields a magnification of 100, and the pixel size of the camera is  $20 \mu\text{m}$ .

The sequence to map the phases and amplitudes of the beam worked as expected and revealed smooth phase and amplitude profiles. Fig. 4.3 shows exposures of the sequences of three interference patterns, shifted by  $2\pi/3$  from one to the next, for two different superpixel pairs. The single visible microsphere shows a strong interference contrast, but the background is quite visible, too (possibly dust or residues from the drying process).

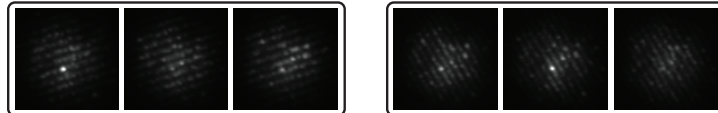


Figure 4.3: Microsphere calibration sequence: three-phase-measurement for two patch pairs.

The background makes it difficult to measure beam cross sections precisely, because the CCD camera captures the convolution of the beam profile with the point-spread-function of the imaging system, and a scan like in the previous chapter yields the actual beam profile convolved with the spatial signal-noise-distribution. The latter is illustrated in fig. 4.4, where the amplitude profile was flattened in the Fourier plane to form a  $\text{sinc}^2$ -beam on the microsphere, and scanned over an area around a single microsphere. The figures shows a dataset on top of the calculated profile. It also includes an attempt to explain the difference between those two by implementing the observed noise floor into the calculations.

Unfortunately, the high precision results from the low-NA setup could not be confirmed conclusively in this test. Nonetheless, it shows the general applicability of the system for such scenarios.

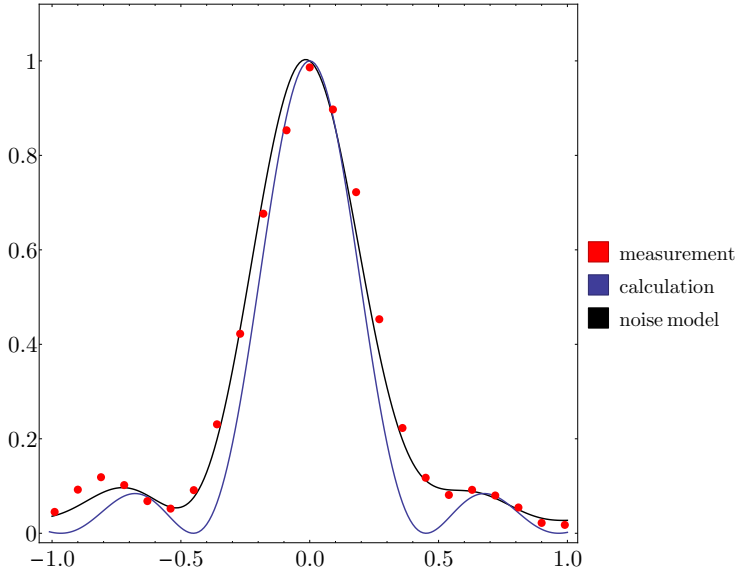


Figure 4.4: Cross section scan of a  $\text{sinc}^2$ -beam. The figure includes a numerical calculation of the profile for infinite signal-to-noise ratio and one that implements the observed noise background.

### 4.3 Quantum Gas Microscope

The holographic DMD system has been tested and benchmarked extensively in both the photodiode setup and the microsphere experiment. The main goal was to make it usable as an extension to our quantum gas microscope. As a first application we wanted to use the system to load atoms into a one-dimensional chain in the optical lattice.

Quantum physics in 1D is of great interest because it exhibits particularly strong correlation. Intuitively, particles confined to one dimension cannot move arbitrarily without passing other particles. Thus, particles interact much stronger even with very short-ranged interactions. While the interacting ground state in higher dimension can be found close to the non-interacting ground state by perturbative means, the interacting ground state in 1D is quite distinct from the non-interacting one and perturbative approaches fail.[47] The established model is that of a *Luttinger liquid*, which was developed for electrons as a replacement of Landau's Fermi liquid theory that is valid in higher dimensions. It takes the long range interactions into account by modelling collective spin- and charge excitations. Most of its concepts are independent of statistics and are applicable for bosonic quantum systems as well.[48] This gives rise to rich physics that can be explored in the Rubidium quantum gas microscope.

Effective one-dimensionality can be achieved in an optical lattice by ramping up the lattice depth in one dimension, so that tunneling between sites in that direction is suppressed[10]. The short interaction range of the atoms leads to pure on-site interactions. In presence of tunneling there is an effective interaction with neighboring lattice sites by *superexchange*, a coherent process of hopping to the neighbor, interacting on-site and hopping back.[49]. Since

increasing the lattice depth prohibits this hopping, it removes any interactions between adjacent lattice columns and decouples them completely.

A problem arises when one tries to read out the occupation numbers for each lattice site. The lattice confinement is so strong that all atoms sit directly on top of each other. In order to see fluorescence, the atoms need to be illuminated, which leads to light assisted collisions, removing atoms pair-wise from the trap before enough fluorescence photons can be collected to detect their presence. Thus, the number on each lattice site is reduced to its parity (0 or 1).[50]

For an experimental measurement of correlation functions we need the ability of reading out absolute occupation numbers for a 1D chain of atoms. The parity projection can be prevented by expanding the 1D gas in the transverse direction, so that the atomic spacing becomes larger than the range of light assisted collisions. In order to do this we need to start with a single 1D gas, compared to the array of 1D gases one gets by simply ramping up the transverse lattice potential.

This is the first goal of our holographic DMD setup. The idea is to create a potential that traps atoms in a tightly confined line. The experimental sequence consists of preparing a 2D Mott Insulator state in the lattice, then applying the line potential and ramping down the transverse lattice so that all atoms outside of the line trap are released, and finally switching back from the line to the transverse lattice. Subsequently, the DMD can be used to create solid walls on both sides of the line to confine the remaining atoms to a well-defined number of lattice sites.

## Setup

We use a blue-detuned laser at 763 nm that is brought into a flattop shape along the atomic line and a Hermite-Gaussian-1 transverse to it in order to trap atoms in the middle of this repulsive double wall (fig. 4.6). The subsequent end-walls are a pair of Gaussian beams aimed at the lattice sites that form the boundary for the chain.

The extreme aspect ratio of the target beam profile leads to laser power issues when created purely by modulations on the DMD. Due to the reciprocal relationship between image and Fourier plane, an aspect ratio of e.g. 40:1 translates into a Fourier pattern that uses only 1/40 of the full aperture. Combined with the losses of 95% from diffraction, this does not leave us with enough laser power to create sufficiently strong potentials.

Our solution is to squeeze the illuminating beam to an aspect ratio of 1:10 by using a cylindrical telescope. This way more light is concentrated on the relevant region on the DMD. This line beam does not have high frequency components in the longitudinal direction in the atom plane. The tightly confined end stopps, however, need these components and require the full aperture in the Fourier plane. For this reason, we use two illumination channels, one on each side of the DMD normal, one of which is strongly elliptical and one of which is circular. Both channels use the same laser, which is fibre-coupled to either one of the two by AOMs (*acusto-optical modulators*).

The optical setup is depicted in fig. 4.5. In each illumination channel, the laser light from the optical fibre is first cleaned up in frequency and polarization by a bandpass filter (BP) and a polarizing beam splitter (PBS). A small portion of the light is then reflected out the beam by a beam sampler and focused onto

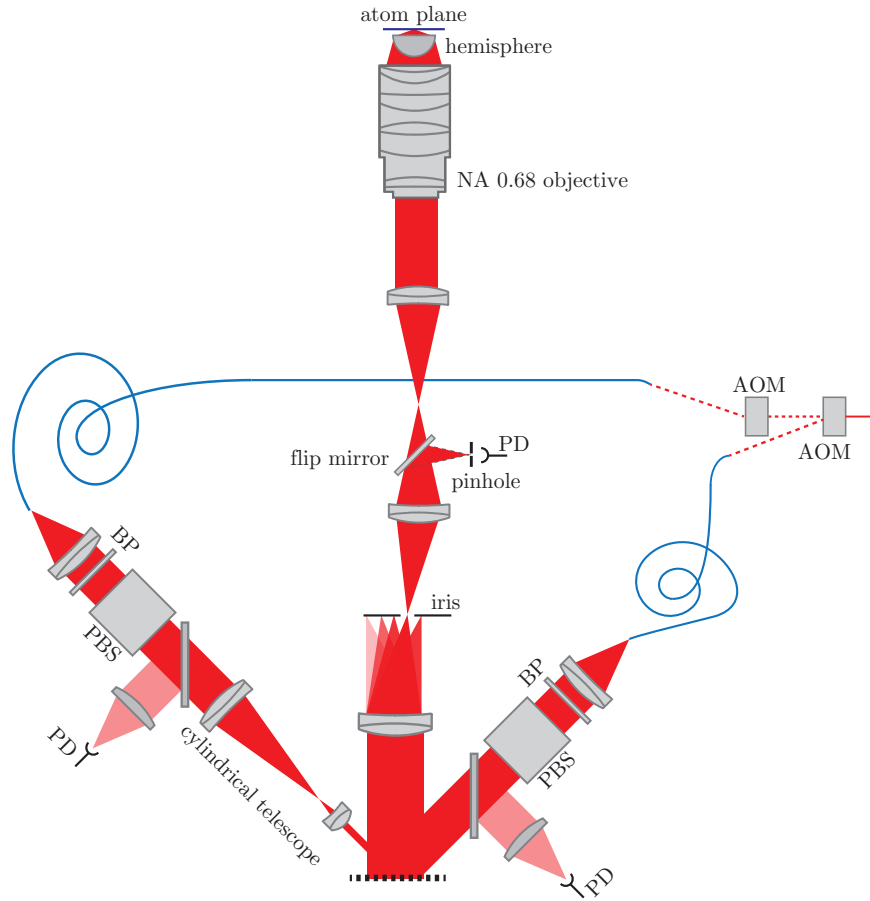


Figure 4.5: Simplified optical setup: Both illumination channels are cleaned up by a bandpass filter (BP) for frequency and a polarizing beamsplitter (PBS) for polarization and intensity-stabilized by the feedback of a photo diode (PD). In a first intermediate image plane all but one diffraction orders are blocked, in a second one a flip mirror allows to reflect the beam onto a photo diode behind a pinhole. The light field is then imaged onto the atom plane. Objective and hemisphere give an effective NA of 0.8.

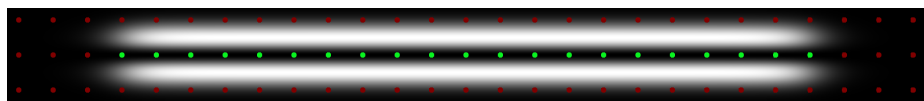


Figure 4.6: The atom trap is shaped as a flattop in one direction and a double-walled Hermite-Gaussian in the other. Green and red dots indicate trapped and untrapped atoms, respectively.

a photo diode, that gives a feedback signal for intensity stabilization. The DMD is illuminated at an angle of  $\pm 24^\circ$ , so that both channels give a beam in the direction of the DMD normal (the mirror tilt is  $\pm 12^\circ$ ). An iris is employed in the first intermediate image plane to select the  $+1^{\text{st}}$  diffraction order. In another intermediate image plane, a hinge-mounted flip mirror allows to redirect the focused beam onto a pinhole with a photodiode, the need of which will be explained in the following section. Finally, the beam is strongly demagnified by an objective with a numerical aperture of 0.68 followed by a glass hemisphere, which increases the effective NA to 0.8.

### Beam Mapping

The phase and amplitude mapping scheme presented before consists in creating interference fringes and reading out intensities. Since the blue-detuned light that we use expels the atoms from their sites, we do not get any fluorescent light from them, so that this scheme fails, and a modification is necessary.

We do the calibration in two steps. First, we run the original sequence using a photo diode behind a pinhole in an intermediate image plane, where we already get all aberrations up to this plane, as well as the amplitude profile. Applying these corrections, we run a second calibration by looking at the interference patterns on the atom.

In this second step, pairs of patches along the line are displayed on the DMD. The atoms are prepared in a superfluid state (weak lattice that allows tunneling), before the laser power for the DMD is ramped up. The atoms then redistribute themselves along the minima of the interference pattern of the two beam patches. We cannot read out fluorescence intensities of single atoms, as we did with the photodiode, so we fit a phase to the distribution of atoms on a finite area instead (fig. 4.8).

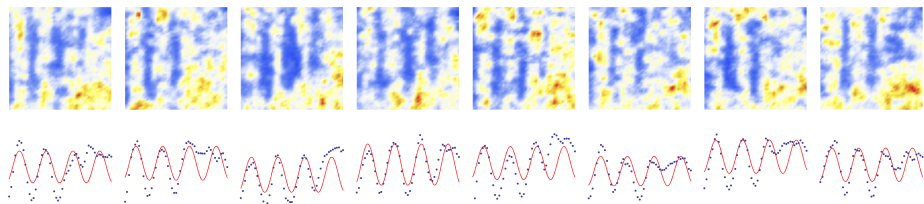


Figure 4.7: Subset of the calibration data showing interference fringes including a phase fit.

The original mapping sequence had a stationary reference patch and yielded phases relative to the phase of this central patch. One consequence of a stationary reference patch is that the period of the resulting interference pattern changes roughly by a factor 10 between a close pair and a distant pair. On the atoms, the scale changes between two and several lattice sites, which makes it difficult to fit the phase. For this reason, the mapping sequence was changed to pairs of equal distance, or a reference patch that moves along with the sampling patch. The down-site is the loss of a universal reference phase.

Correct phase relations can be recovered by fitting the raw data to differences of polynomials

$$f(x) = p(x + \Delta) - p(x) \quad (4.1)$$

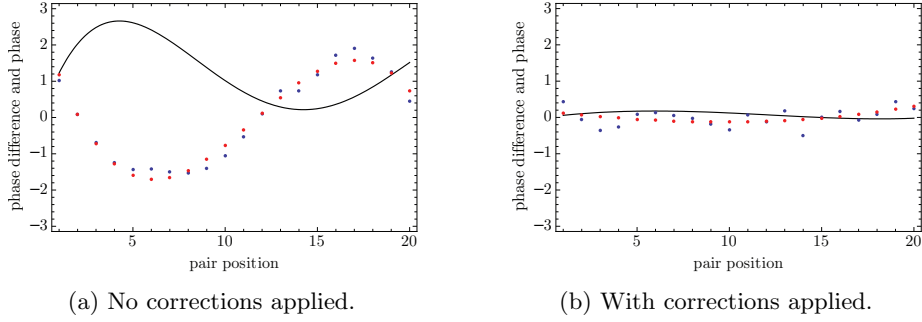


Figure 4.8: Data from the line calibration on the atoms before and after corrections: phase differences (blue dots), polynomial fit (red dots) and reconstructed phase profile (black line).

where

$$p(x) = \sum_{n=0}^N a_n x^n \quad (4.2)$$

is a polynomial of order  $N$ , whose parameters are to be determined, and  $\Delta$  is the Fourier plane spacing between the pairs. The arbitrary definition of phase 0 corresponds to a constant offset in the phase differences, or a tilt in the reconstructed phase map ( $a_1$ ), and can be dropped. Fig. 4.8a depicts the phase profile that was measured this way along the line.

Repeating the phase mapping with those corrections applied show a residual phase error of  $\lambda/50$  (fig. 4.8b).

## Results

After canceling all aberrations, the line potential can be created and fitted to the lattice geometry by finding the right translational and rotational parameters.4.9 The result is a perfect line that is occupied by one atom per lattice site with high fidelity.

Fig. 4.9 shows data from this fitting procedure, averaged over 5 measurements and fitted to lattice positions.

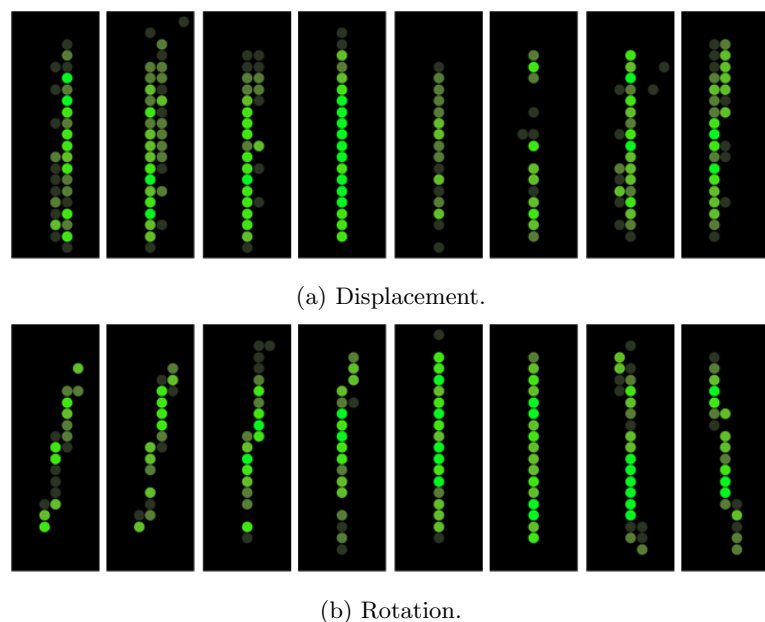


Figure 4.9: Alignment procedure for the line trap.

# Conclusion

I have shown how a digital micromirror device can be used holographically to make a map of the phase and amplitude profile of a beam, and how this information can be used to improve optical performance and to create arbitrary beam shapes. Since this scheme only requires a point detector, it can be applied in-situ for experiments on ultracold atoms in optical lattices, trapped ions or NV centers.

In the pursuit of universal quantum simulators or quantum computers, this could prove to be a useful tool. The strength of the system lies in its ability to steer beams with a precision orders of magnitudes below the lattice spacing and produce shapes with very high signal-to-noise ratios. Diffraction-limited performance and beam wings suppressed to  $10^{-4}$  make it particularly well suited for single site addressing, where the calibration and aiming is mostly automated. (Single site addressing schemes were used before[11], but the holographic SLM makes its application easier, more precise and more universal.) The ability to address single particles in a many-body system to induce state transition or expel them from their location is an important part of the preparation of arbitrary input states for quantum computers.

Furthermore, the system can be used to engineer Hamiltonians by projecting potentials. I have shown that the beam quality deteriorates with an increasing number of features on the desired profile, and direct imaging from an SLM to the atom plane can lead to better results for very complex structures. However, there is a significant subset of beam shapes where the holographic DMD outperforms its image plane counterpart.

Ideally, one would combine the two approaches and switch between or join both systems to get a step closer to high-precision, universal beam shaping.



# Appendices



# Appendix A

## Dressed State Picture

In the study of ultracold atoms Alkali atoms such as Lithium or Rubidium are very popular, because their electronic level structure is relatively simple[23, ch. 8]. With this sparse energy spectrum, the atom can be approximated as a two-level-system, when the energy scales in an experiment are within a small range, that is close to only a single atomic transition. This approximation yields an analytic solution to the interaction problem of atoms and light.

Following [19, ch. 7], I will treat the problem semiclassically, which means that the interaction of a quantum two-level-system with a classical oscillating electric field will be considered.

In order to understand the effect of the interaction, we need to solve the time-dependent Schrödinger equation

$$i\hbar \frac{\partial \Psi}{\partial t} = H\Psi, \quad (\text{A.1})$$

where the Hamiltonian

$$H(t) = H_0 + H_I(t) \quad (\text{A.2})$$

is composed of the operator  $H_0$  describing the unperturbed two-level-system and the time-dependent interaction term  $H_I$ . We will use the Eigenstates of the unperturbed Hamiltonian

$$|n\rangle(t) = |n\rangle e^{-iE_n t/\hbar} \quad (\text{A.3})$$

with

$$H_0 |n\rangle = E_n |n\rangle \quad (\text{A.4})$$

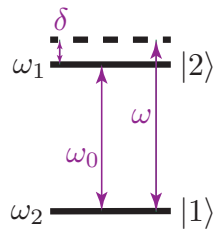


Figure A.1: Energy levels in a two-level-system.

as a basis for the perturbed system, so that any state can be described by

$$|\Psi\rangle(t) = c_1(t)|1\rangle e^{-iE_1 t/\hbar} + c_2(t)|2\rangle e^{-iE_2 t/\hbar} \quad (\text{A.5})$$

with  $|c_1(t)|^2 + |c_2(t)|^2 = 1 \forall t$ . In this basis, eq. A.1 reads

$$\begin{aligned} i\hbar \frac{\partial \Psi}{\partial t} &= (i\hbar\dot{c}_1(t) + E_1 c_1(t))|1\rangle e^{-iE_1 t/\hbar} \\ &\quad + (i\hbar\dot{c}_2(t) + E_2 c_2(t))|2\rangle e^{-iE_2 t/\hbar} \\ &= c_1(t)(E_1 + H_{\text{I}})|1\rangle e^{-iE_1 t/\hbar} + c_2(t)(E_2 + H_{\text{I}})|2\rangle e^{-iE_2 t/\hbar}, \end{aligned} \quad (\text{A.6})$$

or, simplified and introducing frequencies  $\omega_n = E_n/\hbar$

$$i(\dot{c}_1(t)|1\rangle e^{-i\omega_1 t} + \dot{c}_2(t)|2\rangle e^{-i\omega_2 t}) = c_1(t)\frac{H_{\text{I}}}{\hbar}|1\rangle e^{-i\omega_1 t} + c_2(t)\frac{H_{\text{I}}}{\hbar}|2\rangle e^{-i\omega_2 t}. \quad (\text{A.7})$$

Since in the cases of interest the size of an atom is much smaller than a wavelength of the electric field  $\vec{E} = \vec{E}_0 \cos(\omega t)$ , we can assume the electromagnetic vector potential to be constant over the extent of the atom. In this approximation, the interaction reduces to a dipole interaction[23, ch. 4.3]

$$H_{\text{I}}(t) = -\vec{d}\vec{E}_0 \cos(\omega t), \quad (\text{A.8})$$

where  $\vec{d} = -e\vec{r}$  denotes the electric dipole operator. It only connects states with opposite parity due to its own negative parity[19, ch. 2], so that we have matrix elements

$$\begin{aligned} 0 &= \langle 1 | \vec{d} | 1 \rangle = \langle 2 | \vec{d} | 2 \rangle \text{ and} \\ \vec{d}_{12} &\equiv \langle 2 | \vec{d} | 1 \rangle = \left( \langle 1 | \vec{d} | 2 \rangle \right)^*. \end{aligned} \quad (\text{A.9})$$

Let us further define  $d = \vec{d}_{12} \cdot \vec{\epsilon}$  for simplicity, where  $\vec{\epsilon} = \vec{E}_0/E_0$  is the polarization vector of the electric field. Now, applying  $\langle 1 |$  and  $\langle 2 |$  to eq. A.7 from the left, we get

$$\begin{aligned} i\dot{c}_1(t) &= \Omega_0 \cos(\omega t) e^{-i\omega_0 t} c_2(t) = \frac{\Omega_0}{2} \left( e^{i(\omega-\omega_0)t} + e^{-i(\omega+\omega_0)t} \right) c_2(t) \\ i\dot{c}_2(t) &= \Omega_0 \cos(\omega t) e^{i\omega_0 t} c_1(t) = \frac{\Omega_0}{2} \left( e^{i(\omega+\omega_0)t} + e^{-i(\omega-\omega_0)t} \right) c_1(t) \end{aligned} \quad (\text{A.10})$$

where  $\omega_0 = \omega_2 - \omega_1$  is the energy difference between the two levels and  $\Omega_0 = dE_0/\hbar$  is the *Rabi frequency*.

In this derivation we are interested in the near-resonant case, i.e.  $\omega \approx \omega_0$ . This means, that the frequency  $\omega + \omega_0 \approx 2\omega$  in the equation above is oscillating so fast that it averages to 0 quickly over the relevant time scales, while the dynamics of the interaction are contained in the detuning  $\delta = \omega - \omega_0 \ll \omega$ . This is called *rotating-wave approximation* and allows us to drop the fast oscillating part, leaving us with

$$\begin{aligned} i\dot{c}_1(t) &= \frac{\Omega_0}{2} e^{i\delta t} c_2(t) \\ i\dot{c}_2(t) &= \frac{\Omega_0}{2} e^{-i\delta t} c_1(t). \end{aligned} \quad (\text{A.11})$$

We can now switch to a rotating frame to get rid of the external time dependence in the exponential by defining

$$\begin{aligned}\tilde{c}_1(t) &= e^{-i\delta t/2} c_1(t) \\ \tilde{c}_2(t) &= e^{i\delta t/2} c_2(t).\end{aligned}\quad (\text{A.12})$$

In this frame our set of differential equations reads

$$\begin{aligned}i\dot{\tilde{c}}_1 &= i \frac{d}{dt} \left( e^{-i\delta t/2} c_1(t) \right) \\ &= \frac{\delta}{2} e^{-i\delta t/2} c_1(t) + e^{-i\delta t/2} \frac{\Omega_0}{2} e^{i\delta t} c_2(t) \\ &= \frac{\delta}{2} \tilde{c}_1(t) + \frac{\Omega_0}{2} \tilde{c}_2(t) \\ i\dot{\tilde{c}}_2 &= -\frac{\delta}{2} \tilde{c}_2(t) + \frac{\Omega_0}{2} \tilde{c}_1(t),\end{aligned}\quad (\text{A.13})$$

or, more compactly,

$$\frac{d}{dt} \begin{pmatrix} \tilde{c}_1(t) \\ \tilde{c}_2(t) \end{pmatrix} = \frac{i}{2} \begin{pmatrix} -\delta & \Omega_0 \\ \Omega_0 & \delta \end{pmatrix} \begin{pmatrix} \tilde{c}_1(t) \\ \tilde{c}_2(t) \end{pmatrix}. \quad (\text{A.14})$$

One result we can derive from this is for the case of resonant light ( $\delta = 0$ ). Picking  $\tilde{c}_1(0) = 1$  and  $\tilde{c}_2(0) = 0$  as initial conditions, which corresponds to the ground state  $|1\rangle$  of the unperturbed system, we get the solution

$$\begin{aligned}|c_1|^2 &= \cos^2 \left( \frac{\Omega_0 t}{2} \right) \\ |c_2|^2 &= \sin^2 \left( \frac{\Omega_0 t}{2} \right).\end{aligned}\quad (\text{A.15})$$

Without detuning, the light field coherently shifts the population between the ground-state  $|1\rangle$  and the excited state  $|2\rangle$ . This is called *Rabi oscillation*. Thus, we can use light to excite and de-excite electronic states in an atom. For non-resonant light, the populations oscillate with the generalized Rabi frequency  $\Omega = \sqrt{\Omega_0^2 + \delta^2}$  and with the damped amplitude

$$\frac{\Omega_0^2}{\Omega^2} \approx 1 - \frac{\delta^2}{\Omega^2}. \quad (\text{A.16})$$

We get another important result when we calculate the new eigenenergies of the combined atom-light system. They are found to be

$$\tilde{E}_{1/2} = \pm \Omega = \pm \frac{1}{2} \sqrt{\delta^2 + \Omega_0^2} \approx \pm \left( \frac{\delta}{2} + \frac{\Omega_0^2}{4\delta} \right) \quad (\text{A.17})$$

where the approximation is valid for large detunings (i.e.  $|\delta| \gg \Omega_0$ , but still  $|\delta| \ll \omega$ ). We changed basis when we switched to the rotating frame, so our unperturbed energies are not  $E_{1/2}$  anymore, but  $\pm\delta$ . This means, the oscillating electric field leads to the so-called *AC-Stark* or *light shift* of the energy levels

$$\Delta\omega_{\text{light}} = \tilde{E}_1(\Omega_0) - \tilde{E}_1(0) = \frac{\Omega_0^2}{4\delta} \quad (\text{A.18})$$

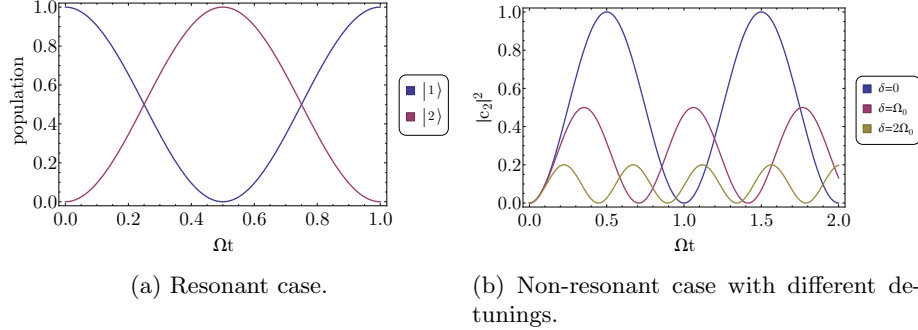


Figure A.2: Rabi oscillations.

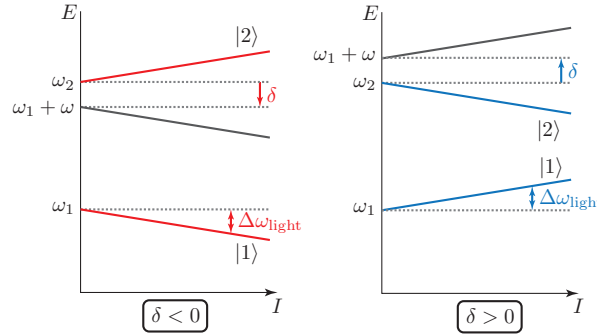


Figure A.3: AC Stark shift as function of the light intensity for positive and negative detuning.

The corresponding eigenstates are commonly called *dressed states*, since we are dealing with a compound atom-light system.

The meaning of that light shift is, that detuned light acts as an effective potential for the atom. The effect of this shift will depend on the sign of the detuning - red-detuned light ( $\delta < 0$ ) will create an attractive potential while blue-detuned light ( $\delta > 0$ ) will create a repulsive one. The light shift is proportional to the square of the Rabi frequency, which is proportional to the strength of the electric field, which in turn is proportional to the square root of the light intensity. Thus, the effective potential is proportional to the local light intensity:

$$U_{\text{dip}} = \Delta\omega_{\text{light}} = \frac{\Omega_0^2}{4\delta} = \frac{d^2 E_0^2}{4\hbar^2 \delta} = \frac{2d^2}{4\hbar^2 c\epsilon_0 \delta} I. \quad (\text{A.19})$$

## Appendix B

# The 30-minute Guide to Fourier Optics

A very useful concept of optics is that of an imaging system. An imaging system collects light from an object in one plane (the object plane) and reproduces a similar intensity profile in another plane (the image plane). A naively *ideal* system maps each point in the object plane to one point in the image plane in a linear and isotropic way, so that

$$I(\vec{x}_o) \rightarrow I(\vec{x}_i) = I(m\vec{x}_o) \quad (\text{B.1})$$

where  $I$  denotes the intensity distribution function,  $\vec{x}_{o/i}$  is a set of coordinates in the object and image plane, respectively, and  $m$  is the (possibly negative) magnification.

Since Ernst Abbe came up with his theory of image formation in 1873, we have a good understanding of why physical imaging systems will always fall short of this ideal performance. His insight was that the image performance is ultimately limited by diffraction: the methods of ray optics, that were exclusively utilized before, are only an approximation to the full story.

In order to get to that result and others, which shall be important for this thesis, I will briefly review the model of the angular spectrum. This approach is fairly far from the original formulation of diffraction theory, but comes without its cumbersome geometrical calculations, can be fit into just a few pages and elegantly yields all the results we need. (It is also a powerful way to calculate diffraction patterns when solving the Kirchhoff diffraction integral is computationally too hard.[51]) I will follow [33] throughout this section in argumentation and (though not pedantically) notation.

### Angular Spectrum

The brilliant insight of the angular spectrum approach is the close resemblance between a Fourier transform and a decomposition into natural propagation modes. A Fourier transform

$$\mathfrak{F}\{g\}(f_X) = G(f_X) = \int_{\mathbb{R}} g(x) e^{-i2\pi f_X x} dx \quad (\text{B.2})$$

yields a function's frequency spectrum, so that it can be written as an integral over plane waves  $\exp(i2\pi f_X x)$ ,

$$g(x) = \mathfrak{F}^{-1}\{G\}(x) = \int_{\mathbb{R}} G(f_X) e^{i2\pi f_X x} df_X. \quad (\text{B.3})$$

In order to fully - within a scalar theory - understand the propagation of a light field, we can now look at an easier problem, the propagation of the plane waves that correspond to the light field's frequency components.

Let us assume we have a coherent, monochromatic light field propagating in the positive z-direction. The spatially-varying complex light field will be denoted by  $U(x, y, z)$ , its frequency spectrum by  $A(f_X, f_Y; z)$  (this is a 2D Fourier transform in a plane perpendicular to the direction of propagation). Given the light field across the plane at  $z = 0$  is

$$U(x, y, 0) = \iint_{\mathbb{R}^2} A(f_X, f_Y; 0) e^{i2\pi(f_X x + f_Y y)} df_X df_Y, \quad (\text{B.4})$$

the question we want to answer is what it will be at a parallel plane at  $z > 0$ .

A propagating plane wave is of the form

$$p(\vec{r}, t) = \exp(i\vec{k} \cdot \vec{r} - \omega t) \quad (\text{B.5})$$

with  $\vec{k} = k \cdot (\alpha, \beta, \gamma)$ ,  $k = 2\pi/\lambda$  and  $\omega = kc$ .  $(\alpha, \beta, \gamma)$  is a set of direction cosines which need to fulfill the condition  $\alpha^2 + \beta^2 + \gamma^2 = 1$ . With the identifications

$$\begin{aligned} \alpha &= \lambda f_X \\ \beta &= \lambda f_Y \\ \gamma &= \sqrt{1 - (\lambda f_X)^2 - (\lambda f_Y)^2} \end{aligned} \quad (\text{B.6})$$

we can interpret the Fourier components as plane waves of the same wavelength traveling in different directions. This is why the function

$$A\left(\frac{\alpha}{\lambda}, \frac{\beta}{\lambda}; z\right) = \iint_{\mathbb{R}^2} U(x, y, z) \exp\left\{-i2\pi\left(\frac{\alpha}{\lambda}x + \frac{\beta}{\lambda}y\right)\right\} dx dy \quad (\text{B.7})$$

is called the *angular spectrum* of the light field  $U(\vec{r})$ .

Since we are studying a propagation phenomenon in a source-free region of space, the Helmholtz equation

$$\nabla^2 U(\vec{r}) + k^2 U(\vec{r}) = 0 \quad (\text{B.8})$$

can help us unveil the dynamics of the angular spectrum. For this purpose, we write  $U(\vec{r})$  as

$$U(x, y, z) = \iint_{\mathbb{R}^2} A\left(\frac{\alpha}{\lambda}, \frac{\beta}{\lambda}; z\right) \exp\left\{i2\pi\left(\frac{\alpha}{\lambda}x + \frac{\beta}{\lambda}y\right)\right\} d\frac{\alpha}{\lambda} d\frac{\beta}{\lambda}, \quad (\text{B.9})$$

so that the Helmholtz equation yields

$$\begin{aligned}
0 &= \nabla^2 U(x, y, z) + k^2 U(x, y, z) \\
&= \iint_{\mathbb{R}^2} \left\{ \frac{d^2}{dx^2} + \frac{d^2}{dy^2} + \frac{d^2}{dz^2} + k^2 \right\} \\
&\quad \times \left[ A \left( \frac{\alpha}{\lambda}, \frac{\beta}{\lambda}; z \right) \exp \left\{ i2\pi \left( \frac{\alpha}{\lambda}x + \frac{\beta}{\lambda}y \right) \right\} \right] d\frac{\alpha}{\lambda} d\frac{\beta}{\lambda} \\
&= \iint_{\mathbb{R}^2} \left\{ -\left( \frac{2\pi}{\lambda} \right)^2 \alpha^2 - \left( \frac{2\pi}{\lambda} \right)^2 \beta^2 + \frac{d^2}{dz^2} + \left( \frac{2\pi}{\lambda} \right)^2 \right\} \\
&\quad \times \left[ A \left( \frac{\alpha}{\lambda}, \frac{\beta}{\lambda}; z \right) \exp \left\{ i2\pi \left( \frac{\alpha}{\lambda}x + \frac{\beta}{\lambda}y \right) \right\} \right] d\frac{\alpha}{\lambda} d\frac{\beta}{\lambda} \quad (\text{B.10})
\end{aligned}$$

where the Leibniz rule has been used to get from the first to the second line. Now, we are left with the differential equation

$$\frac{d^2}{dz^2} A \left( \frac{\alpha}{\lambda}, \frac{\beta}{\lambda}; z \right) + \left( \frac{2\pi}{\lambda} \right)^2 [1 - \alpha^2 - \beta^2] A \left( \frac{\alpha}{\lambda}, \frac{\beta}{\lambda}; z \right) = 0 \quad (\text{B.11})$$

with the simple solution

$$A \left( \frac{\alpha}{\lambda}, \frac{\beta}{\lambda}; z \right) = A \left( \frac{\alpha}{\lambda}, \frac{\beta}{\lambda}; 0 \right) \exp \left( i \frac{2\pi}{\lambda} \sqrt{1 - \alpha^2 - \beta^2} z \right) \quad (\text{B.12})$$

This is exactly what one might have intuitively expected from the propagation of plane waves: pathlengths vary due to distinct directions so that components collect individual phase shifts.

I called  $\alpha$ ,  $\beta$  and  $\gamma$  direction cosines though the conditions  $(\alpha, \beta, \gamma) \in [0, 1]^3$  was not mathematically enforced - until now: according to eq. B.12, only components with  $\alpha^2 + \beta^2 < 1$  are propagating modes. For  $\alpha^2 + \beta^2 > 1$ , the solution turns into the exponentially decaying function

$$A \left( \frac{\alpha}{\lambda}, \frac{\beta}{\lambda}; z \right) = A \left( \frac{\alpha}{\lambda}, \frac{\beta}{\lambda}; 0 \right) \exp \left( -\frac{2\pi}{\lambda} \sqrt{\alpha^2 + \beta^2 - 1} z \right) \quad (\text{B.13})$$

that describes *evanescent* waves.

We can not return from direction cosines to Fourier coefficients. The factor

$$H(f_X, f_Y) = \begin{cases} \exp \left( -2\pi \frac{z}{\lambda} \sqrt{(\lambda f_X)^2 + (\lambda f_Y)^2 - 1} \right) & \text{for } \sqrt{f_X^2 + f_Y^2} > \frac{1}{\lambda} \\ 0 & \text{else} \end{cases} \quad (\text{B.14})$$

from eq. B.13 is called *transfer function* and acts as a propagator on the frequency spectrum. This yields our first import result: frequency components with

$$f_X^2 + f_Y^2 > \frac{1}{\lambda^2} \quad (\text{B.15})$$

are exponentially suppressed. In the convenient language of signal processing, the wavelength of the light imposes a fundamental limit to the bandwidth of the optical system. The finest structure that can be resolved in real space depends on the highest frequency component that is passed through. In a conventional optical system, the wavelength defines this threshold.

In order to get the amplitude distribution in a plane at  $z > 0$  we need to calculate the inverse Fourier transform of the propagated angular spectrum,

$$\begin{aligned} U(x, y, z) &= \iint_{\mathbb{R}^2} A\left(\frac{\alpha}{\lambda}, \frac{\beta}{\lambda}; 0\right) \exp\left(-\frac{2\pi}{\lambda}\sqrt{\alpha^2 + \beta^2 - 1}z\right) \\ &\quad \times \exp\left(i2\pi\left(\frac{\alpha}{\lambda}x + \frac{\beta}{\lambda}y\right)\right) d\frac{\alpha}{\lambda} d\frac{\beta}{\lambda} \\ &= \iint_{\mathbb{R}^2} A\left(\frac{\alpha}{\lambda}, \frac{\beta}{\lambda}; 0\right) \\ &\quad \times \exp\left(i\frac{2\pi}{\lambda}\left(\alpha x + \beta y - \sqrt{\alpha^2 + \beta^2 - 1}z\right)\right) d\frac{\alpha}{\lambda} d\frac{\beta}{\lambda}. \end{aligned} \quad (\text{B.16})$$

## Diffraction

Diffraction describes the effect of light rays not following their geometrical paths. Its observation was the first hint that ray optics are incomplete and that lead to the development of wave optics. The key discoveries were that there could be light in the geometrical shadow region of obstacles and that adding light could reduce the intensity in some cases. We want to review the effect of an opaque mask on the propagation of a light beam.

The convolution theorem states that the convolution of two functions in the space domain corresponds to the product of the two functions in the frequency domain[33, ch. 2]:

$$\mathfrak{F}\{g(x) * h(x)\} = \mathfrak{F}\left\{\int_{\mathbb{R}} g(\xi)h(x - \xi) d\xi\right\} = G(f_X)H(f_X) \quad (\text{B.17})$$

where  $*$  denotes the convolution and capital letters represent the Fourier transformed functions. We will make use of that statement to get the angular spectrum of the light field after passing through the mask. For this we define the amplitude-transmission-function of the mask

$$t(x, y) = \frac{U_t(x, y, 0)}{U_i(x, y, 0)} \quad (\text{B.18})$$

as the quotient of the transmitted light field  $U_t$  and the illuminating light field  $U_i$ . Solving for  $U_t$  and going to the frequency domain, we get

$$A_t\left(\frac{\alpha}{\lambda}, \frac{\beta}{\lambda}; 0\right) = A_i\left(\frac{\alpha}{\lambda}, \frac{\beta}{\lambda}; 0\right) * T\left(\frac{\alpha}{\lambda}, \frac{\beta}{\lambda}\right). \quad (\text{B.19})$$

For the case of illumination by plane waves parallel to the mask, i.e.

$$A_i\left(\frac{\alpha}{\lambda}, \frac{\beta}{\lambda}; 0\right) = \delta\left(\frac{\alpha}{\lambda}, \frac{\beta}{\lambda}\right) \quad (\text{B.20})$$

eq. B.19 simplifies to

$$A_t\left(\frac{\alpha}{\lambda}, \frac{\beta}{\lambda}; 0\right) = \delta\left(\frac{\alpha}{\lambda}, \frac{\beta}{\lambda}\right) * T\left(\frac{\alpha}{\lambda}, \frac{\beta}{\lambda}\right) = T\left(\frac{\alpha}{\lambda}, \frac{\beta}{\lambda}\right), \quad (\text{B.21})$$

so the angular spectrum behind the mask is just given by its Fourier transform. This allows us to apply the propagator in eq. B.16 to the angular spectrum of the mask in order to calculate the diffracted amplitude distribution in another plane at  $z > 0$ .

For this thesis I will mostly be dealing with the far-field or *Fraunhofer* limit of diffraction describing the case of large  $z$  compared to the size of the diffracting structure. We can use the *stationary phase approximation*[52, A. III] to calculate the limit of integral B.16 for  $z \rightarrow \infty$ . The basic argument is, that, given an integral

$$\lim_{z \rightarrow \infty} \int_{\mathbb{R}} g(x) \exp(izf(x)) dx, \quad (\text{B.22})$$

the complex oscillation will be so fast that phases add up incoherently and average to zero everywhere except for the stationary points of  $f(x)$ , i.e. those satisfying  $df(x)/dx = 0$ .

We want to calculate the amplitude at a point  $\vec{r}_\infty$  infinitely far from the mask. For this we define the unit vector  $\vec{u} = (x_\infty/r, y_\infty/r, z_\infty/r)$  with  $r = |\vec{r}_\infty|$ . With this, eq. B.16 reads

$$U_\infty(u_x, u_y) = \lim_{(\frac{r}{\lambda}) \rightarrow \infty} \iint_{\mathbb{R}^2} A\left(\frac{\alpha}{\lambda}, \frac{\beta}{\lambda}; 0\right) \times \exp\left(i2\pi\frac{r}{\lambda}\left(\alpha u_x + \beta u_y - \sqrt{\alpha^2 + \beta^2 - 1} u_z\right)\right) d\frac{\alpha}{\lambda} d\frac{\beta}{\lambda} \quad (\text{B.23})$$

with  $u_z = \sqrt{1 - u_x^2 - u_y^2}$ . The result is[53]

$$U_\infty(u_x, u_y) \propto A\left(\frac{2\pi}{\lambda}u_x, \frac{2\pi}{\lambda}u_y; 0\right) \quad (\text{B.24})$$

We thus see that in the far field the amplitude at a point  $\vec{r}$  is given by the component of the angular spectrum that is traveling to this point, so that there is a one-to-mapping of locations on an infinitely-far screen to Fourier components. In other words, the far-field diffraction pattern of a mask is given by its Fourier transform.

## Lenses

A positive lens is a refractive optical element that focuses a collimated beam to a plane one focal length  $f$  away, as is well known from geometrical optics. In terms of wave optics, the collimated beam is described by a plane wave  $\exp(ikx)$  (ignoring the time dependence), while the focused beam is given by a spherical wave  $\exp(i\phi(\vec{r})) = \exp(i(kr))$  with  $r = \sqrt{x^2 + y^2 + z^2}$ . Thus, the lens turns a flat wavefront into a spherical one, by retarding phase evolution in some parts of the beams more than in others. The imprinted phase profile in the principal plane of the lens is given by

$$\phi(x, y, -f) = k\sqrt{x^2 + y^2 + f^2} \approx k\left(f + \frac{x^2 + y^2}{2f}\right). \quad (\text{B.25})$$

Lenses have an intriguing property. Fig. B.1 illustrates the geometry of a mask placed  $x$  in front of a lens. A plane wave emerging from the mask at some

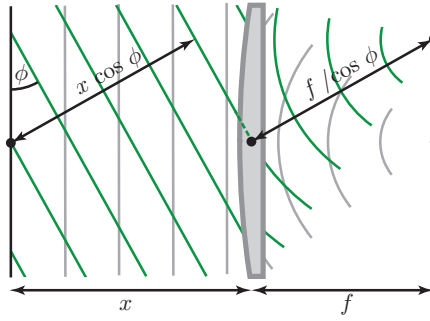


Figure B.1: Path differences for distinct components of the angular spectrum in front of and behind a lens.

angle  $\phi$  will be focused onto the image plane (a distance  $f$  behind the lens). The path length for plane waves from the mask to the lens (i.e. the distance between one plane on the center of the mask and one on the center of the lens, both perpendicular to propagation) is

$$\Delta_1 = x \cos \phi, \quad (\text{B.26})$$

so that the corresponding frequency component will have picked up a phase factor of

$$p_1 = \exp\left(i \frac{2\pi}{\lambda} x \cos \phi\right) \quad (\text{B.27})$$

when it reaches the lens, while the acquired phase factor from the lens to the image plane is

$$p_2 = \exp\left(i \frac{2\pi}{\lambda} \frac{f}{\cos \phi}\right). \quad (\text{B.28})$$

Going to the paraxial approximation

$$\cos \phi \approx 1 - \frac{\phi^2}{2} \quad \text{and} \quad \frac{1}{\cos \phi} \approx 1 + \frac{\phi^2}{2} \quad (\text{B.29})$$

we get a total phase factor of

$$p_1 \cdot p_2 = \exp\left(i \frac{2\pi}{\lambda} (f - x) \frac{\phi^2}{2}\right). \quad (\text{B.30})$$

If we now choose  $x = f$ , then the suffered phase shift will be independent of the propagation angle and thus will be the same for all frequency components of the mask. Since there is further a one-to-mapping of image points to the angle  $\phi$  and hence to the corresponding Fourier component, this setup will create an exact Fourier transform of the mask in the image plane (exact up to the point-spread-function, that will be introduced in the next section). For obvious reasons, the back focal plane containing the mask is called *Fourier plane* in this context.

This can be applied for optical image processing and spatial light modulation. Filtering in the Fourier plane can enhance signals and recover information that is not accessible in the image plane. In the project described in this thesis the frequency spectrum of a beam is modulated in order to get a certain shape in the image plane.

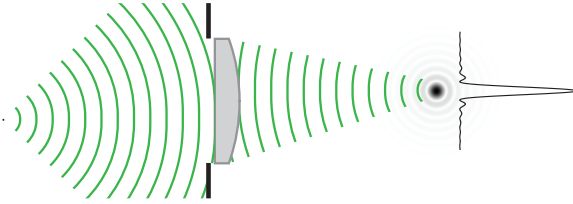


Figure B.2: The finite exit pupil leads to a diffraction effect and generates an Airy disk as the point image.

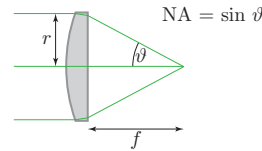


Figure B.3: Aperture and numerical aperture.

## Image Formation

Propagation of light is ultimately described by Maxwell's equations, which are linear differential equations. Because of this, optical setups can be treated as linear systems. This means that in the formation of images we can first calculate the image of a point source, the so-called *impulse response*  $h(x, y; \xi, \eta)$ , where  $x, y$  are coordinates in the image plane and  $\xi, \eta$  are coordinates in the object plane. This function is commonly called *point-spread function (PSF)*. We then get the full image by integrating the impulse response over the object plane:

$$U(x, y) = \iint_{\mathbb{R}^2} U(\xi, \eta) h(x, y; \xi, \eta) d\xi d\eta. \quad (\text{B.31})$$

An optical system can be approximated by a space-invariant system [33, ch. 2], which means that the impulse response depends on relative coordinates only, so that

$$U(x, y) = \iint_{\mathbb{R}^2} U(\xi, \eta) h(x - \xi, y - \eta) d\xi d\eta. \quad (\text{B.32})$$

Hence, the image is the convolution of the object with the PSF. Since  $h(x, y)$  is a space-domain propagator, it is the Fourier transform of the transfer function  $H(f_X, f_Y)$ , which was defined as the Fourier space propagator in eq. B.14.

The afore-mentioned naively-perfect imaging system (eq. B.1) corresponds to

$$h(x, y; \xi, \eta) = \delta^{(2)}(\xi - Mx, \eta - My) \quad (\text{B.33})$$

Considering the bandwidth limitation of the system, the real image of a point will be more broadly distributed, hence the name point-spread function.

The bandwidth is not only limited by the occurrence of evanescent waves above  $f = 1/\lambda$ , but also by the apertures of the optical setup. In an imaging system, entrance and exit pupils describe the maximum extent of a beam that can pass through without clipping. Since this number is finite, diffraction effects need to be taken into account. In fact, careful calculations [33, ch. 5] show, that the PSF will be the Fraunhofer diffraction pattern of the limiting aperture. The far-field pattern of a circular mask is an Airy-disk, so that this will generally be the profile of point-spread-functions (fig. B.2).

If an imaging system transforms a diverging spherical wave from the object plane into a spherical wave converging on the image plane, it is called *diffraction-limited*. Such a system has ideal performance under the restraints of

its geometry, which means that it is limited *only* by diffraction, in contrast to limitations due to imperfections of the setup, which are considered in the next section.

The actual size of the Airy disk in the image plane depends on the focal length  $f$  of the imaging system and its exit pupil diameter  $2r$ , or more specifically their ratio, which is a function of the maximum angle  $\theta$  at which light propagates towards the focus (B.3). For this reason, the *numerical aperture* NA is defined as the sine of this angle. The higher the NA, the broader the light cone and the smaller the feature in the image plane.

In the case of laser light, the aperture is usually not filled homogeneously. Instead, a *Gaussian* beam profile, which is a solution to the source-free Helmholtz equation and thus a stable free-space propagation mode, is more likely to be found:

$$U(r, z) \propto \exp\left(-\frac{r^2}{w(z)^2}\right) \quad (\text{B.34})$$

where  $w(z)$  denotes the waist (radius) of the beam. It is a straight-forward calculation to show that a Gaussian profile is invariant under Fourier transformation, so that focusing a collimated Gaussian beam (a so-called TEM<sub>00</sub>) will give a Gaussian profile in the image plane. The diffraction-limited focus size is

$$2w_0 = \frac{2\lambda}{\pi \text{NA}} \quad (\text{B.35})$$

In our quantum gas microscopes we use lasers close to  $0.780 \mu\text{m}$  with an NA 0.8 objective. This gives rise to spot sizes of about  $0.62 \mu\text{m}$ , compared to a lattice spacing of  $0.68 \mu\text{m}$ .[22]

# Bibliography

- [1] J. R. Karr, J. C. Sanghvi, D. N. Macklin, M. V. Gutschow, J. M. Jacobs, B. Bolival, N. Assad-Garcia, J. I. Glass, and M. W. Covert, “A whole-cell computational model predicts phenotype from genotype,” *Cell*, vol. 150, Issue 2, pp. 389–401, 2012.
- [2] J. R. Primack, “The cosmological supercomputer - how the bolshoi simulation evolves the universe all over again,” *IEEE Spectrum*, 2012.
- [3] *Supercomputing the Climate: NASA’s Big Data Mission.* [http://www.csc.com/cscworld/publications/81769/81773-supercomputing\\_the\\_climate\\_nasa\\_s\\_big\\_data\\_mission](http://www.csc.com/cscworld/publications/81769/81773-supercomputing_the_climate_nasa_s_big_data_mission), 2012.
- [4] R. Feynman, “Simulating physics with computers,” *International Journal of Theoretical Physics*, vol. 21, no. 6-7, pp. 467–488, 1982.
- [5] L. M. Vandersypen, M. Steffen, G. Breyta, C. S. Yannoni, M. H. Sherwood, and I. L. Chuang, “Experimental realization of shor’s quantum factoring algorithm using nuclear magnetic resonance,” *Nature*, vol. 414, no. 6866, pp. 883–887, 2001.
- [6] I. Bloch, J. Dalibard, and S. Nascimbene, “Quantum simulations with ultracold quantum gases,” *Nat Phys*, vol. 8, pp. 267–276, Apr. 2012.
- [7] R. Blatt and C. Roos, “Quantum simulations with trapped ions,” *Nature Physics*, vol. 8, no. 4, pp. 277–284, 2012.
- [8] J. Cai, A. Retzker, F. Jelezko, and M. B. Plenio, “A large-scale quantum simulator on a diamond surface at room temperature,” *Nature Physics*, vol. 9, no. 3, pp. 168–173, 2013.
- [9] A. Aspuru-Guzik and P. Walther, “Photonic quantum simulators,” *Nature Physics*, vol. 8, no. 4, pp. 285–291, 2012.
- [10] J. Simon, W. S. Bakr, R. Ma, M. E. Tai, P. M. Preiss, and M. Greiner, “Quantum simulation of antiferromagnetic spin chains in an optical lattice,” *Nature*, vol. 472, no. 7343, pp. 307–312, 2011.
- [11] C. Weitenberg, M. Endres, J. F. Sherson, M. Cheneau, P. Schausz, T. Fukuhara, I. Bloch, and S. Kuhr, “Single-spin addressing in an atomic mott insulator,” *Nature*, vol. 471, pp. 319–324, Mar. 2011.
- [12] Y. Zhang, Y. Liu, and S. Wang, “Digital mirror device application in reduction of wave-front phase errors,” *Sensors*, vol. 9, no. 4, pp. 2345–2351, 2009.

- [13] S. Popoff, G. Lerosey, R. Carminati, M. Fink, A. Boccara, and S. Gigan, “Measuring the transmission matrix in optics: an approach to the study and control of light propagation in disordered media,” *Physical review letters*, vol. 104, no. 10, p. 100601, 2010.
- [14] M. Cui, “Parallel wavefront optimization method for focusing light through random scattering media,” *Optics letters*, vol. 36, no. 6, pp. 870–872, 2011.
- [15] D. B. Conkey, A. M. Caravaca-Aguirre, and R. Piestun, “High-speed scattering medium characterization with application to focusing light through turbid media,” *Optics express*, vol. 20, no. 2, pp. 1733–1740, 2012.
- [16] C. Becker, P. Soltan-Panahi, J. Kronjger, S. Drscher, K. Bongs, and K. Sengstock, “Ultracold quantum gases in triangular optical lattices,” *New Journal of Physics*, vol. 12, no. 6, p. 065025, 2010.
- [17] V. Lerner, D. Shwa, Y. Drori, and N. Katz, “Shaping laguerre-gaussian laser modes with binary gratings using a digital micromirror device,” *Opt. Lett.*, vol. 37, pp. 4826–4828, Dec 2012.
- [18] Čižmár, Tomáš *et al.*, “In situ wavefront correction and its application to micromanipulation,” *Nature Photonics*, vol. 4, no. 6, pp. 388–394, 2010.
- [19] C. Foot, *Atomic Physics*. Oxford Master Series in Physics, OUP Oxford, 2005.
- [20] R. Grimm, M. Weidemüller, and Y. B. Ovchinnikov, “Optical dipole traps for neutral atoms,” *Advances in atomic, molecular, and optical physics*, vol. 42, pp. 95–170, 2000.
- [21] J. I. Gillen, *The Quantum Gas Microscope*. PhD thesis, Harvard University, 2009.
- [22] W. R. Bakr, *Microscopic Studies of Quantum Phase Transitions in Optical Lattices*. PhD thesis, Harvard University, 2011.
- [23] B. Bransden and C. Joachain, *Physics of Atoms and Molecules*. Pearson Education, Prentice Hall, 2003.
- [24] W. S. Bakr, A. Peng, M. E. Tai, R. Ma, J. Simon, J. I. Gillen, S. Flölling, L. Pollet, and M. Greiner, “Probing the superfluid-tomott insulator transition at the single-atom level,” *Science*, vol. 329, no. 5991, pp. 547–550, 2010.
- [25] C. Pethick and H. Smith, *Bose-Einstein Condensation in Dilute Gases*. Cambridge University Press, 2002.
- [26] T. Fukuhara, A. Kantian, M. Endres, M. Cheneau, P. Schausz, S. Hild, D. Bellem, U. Schollwock, T. Giannarchi, C. Gross, I. Bloch, and S. Kuhr, “Quantum dynamics of a mobile spin impurity,” *Nat Phys*, vol. 9, pp. 235–241, Apr. 2013.
- [27] D. P. DiVincenzo *et al.*, “The physical implementation of quantum computation,” *arXiv preprint quant-ph/0002077*, 2000.

- [28] J. I. Cirac and P. Zoller, “Goals and opportunities in quantum simulation,” *Nat Phys*, vol. 8, pp. 264–266, Apr. 2012.
- [29] M. Nielsen and I. Chuang, *Quantum Computation and Quantum Information*. Cambridge Series on Information and the Natural Sciences, Cambridge University Press, 2000.
- [30] S. Folling, S. Trotzky, P. Cheinet, M. Feld, R. Saers, A. Widera, T. Muller, and I. Bloch, “Direct observation of second-order atom tunnelling,” *Nature*, vol. 448, pp. 1029–1032, Aug. 2007.
- [31] L. Tarruell, D. Greif, T. Uehlinger, G. Jotzu, and T. Esslinger, “Creating, moving and merging dirac points with a fermi gas in a tunable honeycomb lattice,” *Nature*, vol. 483, pp. 302–305, Mar. 2012.
- [32] U.-J. Wiese, “Ultracold Quantum Gases and Lattice Systems: Quantum Simulation of Lattice Gauge Theories,” *ArXiv e-prints*, May 2013.
- [33] J. Goodman, *Introduction To Fourier Optics*. McGraw-Hill physical and quantum electronics series, Roberts & Company Publishers, 2005.
- [34] K. Thorne, *Lecture Notes, "Applications of Classical Physics", Chapter 7*, Caltech. <http://www.pma.caltech.edu/Courses/ph136/yr2004/>, 2004.
- [35] *Polymers and Liquid Crystals*. Case Western Reserve University, <http://plc.cwru.edu/>, 2000.
- [36] D. Armitage, I. Underwood, and S. Wu, *Introduction to Microdisplays*. Wiley Series in Display Technology, Wiley, 2006.
- [37] J. Griffin, B. Matas, and C. de Suberbasaux, *Memory 1996*. Integrated Circuit Engineering Company, 1996.
- [38] M. Douglass, “Lifetime estimates and unique failure mechanisms of the digital micromirror device (dmd),” in *Reliability Physics Symposium Proceedings, 1998. 36th Annual. 1998 IEEE International*, pp. 9–16, 1998.
- [39] Texas Instruments, *DLP Portfolio*.
- [40] C. Palmer, *Diffraction Grating Handbook*. Newport Corporation, 6 ed., 2005.
- [41] B. Deutsch, R. Hillenbrand, and L. Novotny, “Near-field amplitude and phase recovery using phase-shifting interferometry,” *Opt. Express*, vol. 16, no. 2, pp. 494–501, 2008.
- [42] D. Ghiglia and M. Pitts, *Two-dimensional phase unwrapping: theory, algorithms, and software*. Wiley-Interscience publication, Wiley, 1998.
- [43] R. Eschbach and Z. Fan, “Complex-valued error diffusion for off-axis computer-generated holograms,” *Appl. Opt.*, vol. 32, pp. 3130–3136, Jun 1993.
- [44] Texas Instruments, *DLP Series-450 DMD and System Mounting Concepts (DLPA015)*.

- [45] A. Siegman, *Lasers*. University Science Books, 1986.
- [46] B. Wang and J.-i. Anzai, “Redox reactions of ferricyanide ions in layer-by-layer deposited polysaccharide films: a significant effect of the type of polycation in the films,” *Langmuir*, vol. 23, no. 13, pp. 7378–7384, 2007.
- [47] T. Giamarchi, *Quantum Physics in One Dimension*. International Series of Monographs on Physics, Clarendon Press, 2004.
- [48] F. D. M. Haldane, “Effective harmonic-fluid approach to low-energy properties of one-dimensional quantum fluids,” *Phys. Rev. Lett.*, vol. 47, pp. 1840–1843, Dec 1981.
- [49] S. Trotzky, P. Cheinet, S. Flölling, M. Feld, U. Schnorrberger, A. M. Rey, A. Polkovnikov, E. A. Demler, M. D. Lukin, and I. Bloch, “Time-resolved observation and control of superexchange interactions with ultracold atoms in optical lattices,” *Science*, vol. 319, no. 5861, pp. 295–299, 2008.
- [50] W. S. Bakr, J. I. Gillen, A. Peng, S. Flölling, and M. Greiner, “A quantum gas microscope for detecting single atoms in a hubbard-regime optical lattice,” *Nature*, vol. 462, pp. 74–77, Nov. 2009.
- [51] K. Matsushima, H. Schimmel, and F. Wyrowski, “Fast calculation method for optical diffraction on tilted planes by use of the angular spectrum of plane waves,” *J. Opt. Soc. Am. A*, vol. 20, pp. 1755–1762, Sep 2003.
- [52] M. Born, E. Wolf, and A. Bhatia, *Principles of Optics: Electromagnetic Theory of Propagation, Interference and Diffraction of Light*. Cambridge University Press, 1999.
- [53] L. Novotny, *Lecture Notes, "Electromagnetic Fields and Waves"*, Chapter 7, ETH. <http://www.photonics.ethz.ch/en/courses/electrodynamics.html>, 2013.



# Acknowledgement

I want to thank my advisor Markus Greiner for this exciting project and his good guidance. I learned a lot about optics and physics in general from his intuitive and very practical explanations.

I want to give thanks to my lab mates Rajibul Islam, Alex Lukin, “Alex” Ruichao Ma, Philipp Preiss and Eric Tai for their support and cooperation in implementing the DMD system in the quantum gas microscope. I owe special thanks to Alex, Philipp and Rajibul for proofreading this work. The other group members, Sebastian Blatt, Christie Chiu, Florian Huber, Peter Lu, Anton Mazurenko, Max Parsons and Matthew Rispoli were very supportive and always open to discuss physics and made the last year very enjoyable.

Nicholas Schade’s help in dealing with fluorescent microspheres is much appreciated.

In addition, I want to thank Immanuel Bloch for his consent to evaluate this work.



## **Erklärung**

Hiermit erkläre ich, die vorliegende Arbeit selbständig verfasst zu haben und keine anderen als die in der Arbeit angegebenen Quellen und Hilfsmittel benutzt zu haben.

München, 22. September 2013

